Molecular Mass Engineering for Filaments in Material Extrusion Additive Manufacture

*Sierra F. Yost[1], Christian W. Pester[1,2,3], Bryan D. Vogt[1]**

S. F. Yost, Prof. C. W. Pester, Prof. B. D. Vogt
[1]Department of Chemical Engineering, The Pennsylvania State University, University Park, PA 16802, United States
[2] Department of Materials Science and Engineering, The Pennsylvania State University, University Park, PA 16802, United States
[3] Department of Chemistry, The Pennsylvania State University, University Park, PA 16802, United States

*To whom correspondence should be addressed: bdv5051@psu.edu (B.D.V.)

Keywords: fused filament fabrication, PMMA, 3D printing, tensile properties, rheology

3D printing of thermoplastics through local melting and deposition via Material Extrusion Additive Manufacturing provides a simple route to the near net-shape manufacture of complex objects. However, the mechanical properties resulting from these 3D printed structures tend to be inferior when compared to traditionally manufactured thermoplastics. These unfavorable characteristics are generally attributed to the structure of the interface between printed roads. Here, we illustrate how the molecular mass distribution for a model thermoplastic, poly(methyl methacrylate) (PMMA), can be tuned to enhance the Young's modulus of 3D printed plastics. Engineering the molecular mass distribution alters the entanglement density, which controls the strength of the PMMA in the solid state and the chain diffusion in the melt. Increasing the low molecular mass tail increases Young's modulus and ultimate tensile strength of the printed parts. These changes in mechanical properties are comparable to more complex routes previously reported involving new chemistry or nanoparticles. Controlling the molecular mass distribution provides a simple route to improve the performance in 3D printing of thermoplastics that can be as effective as more complex approaches.

1. Introduction

Additive manufacturing (AM) through direct net-shape printing of objects offers the potential for mass customization, reduction in assembly requirements, and new efficient designs that are not possible through traditional manufacture.[1-3] For AM of polymers, there are three primary modalities: (i) vat photopolymerization,[4] where liquid resin is selectively solidified by light, (ii) selective laser sintering, where a semicrystalline polymer powder is locally melted by laser heating to shape the part, and (iii) material extrusion AM (MEAM),[5] where a thermoplastic melt is locally deposited layer-by-layer. Of these, MEAM offers advantages in terms of affordability, ease of operation, and ability to directly translate many thermoplastics used in traditional manufacturing to AM.[6-8] The feedstocks for MEAM range from low cost commodity polyolefins,[9,10] to engineering thermoplastics,[1] to high performance materials, such as polyetheretherketone.[11] Additionally, the use of thermoplastics instead of thermosets, such as those used in vat photopolymerization, offers opportunities to improve the sustainability of the plastics through recycling.[12-15]

Despite these advantages, the commercial adoption of MEAM is challenged by the inferior mechanical properties of MEAM parts when compared to their traditionally manufactured analogs.[3] The extent of the decrease in mechanical performance is strongly dependent on processing details, so significant efforts have focused on optimizing the print conditions for a given plastic to maximize Young's modulus or other physical properties.[16-19] However, this optimization is not universal as details of the printer and the specific filament used impacts the printed properties and their dependencies on processing conditions. An additional drawback to MEAM is the mechanical anisotropy of the printed part.[20,21] This anisotropy is generally attributed to the directionality of the print path and the effectiveness of the welds between printed roads.[22] Processing conditions can promote the weld formation, e.g., increased temperatures (extrusion, bed, environment), reduced layer thickness (that increases the applied

pressure), changes in infill density, and changes in print path (to reduce cooling of previous layers).[23,24] However, physical limitations to these approaches include minimum shape integrity and a minimum layer height.[25] Moreover, these processing approaches generally tend to only decrease, but not eliminate the mechanical anisotropy, albeit some exceptions have been described with highly engineered commercial filaments.[26]

The interface between the printed roads is generally suggested as the origins for mechanical anisotropy.[27] Consequently, modification of the filaments offers opportunities to improve the performance outside of process optimization for MEAM thermoplastic parts. For example, small changes in the chemistry of polyesters can significantly impact the mechanical properties of the printed parts through reductions in the residual alignment of chains from flow induced by the printing process that limit weld formation.[28] An alternative chemistry-driven approach is to introduce a co-monomer that provides non-covalent bonding (e.g., hydrogen bonds) to form a strong weld without the large scale diffusion across the interface to form a strong weld.[29-31] Due to their surface activity, nanoparticles with favorable interactions with the base polymer can also form effective bonds between layers and enhance mechanical performance.[31-35] The strength of the interface can be enhanced by reactive processing to produce covalent bonds at the interfaces,[36] but this is not applicable to all polymers and the production of covalent bonds can adversely impact the recyclability and sustainability of the 3D printing process. Dadmun and coworkers used surface active additives that preferentially segregate to the surface of the filament and strengthen the interfaces between roads.[37,38] However, not all surface-active polymers were effective for enhancing the mechanical properties. The diffusion of polymers, which is one limiting factor for the interface development, can be improved by the addition of plasticizers to increase the interlayer adhesion in 3D printed parts,[39,40] but plasticizers tend to reduce the Young's modulus so there is generally a trade-off with the use of plasticizers. The combination of plasticizer to improve diffusion with reactive filaments to produce covalent

bonds between layers dramatically improves the mechanical performance,[41] but the covalent bonds challenges the recycling of the printed material and tends to be limited in terms of the chemistry where it can be applied.

Pre- and post-processing has been used as an alternative to chemical alteration to the filament to improve properties. As the interfaces between the printed roads is critical, design of filaments with core-shell structure can provide significant improvements in the mechanical performance through changing the nature of the interfaces within the printed parts.[42-46] Core-shell polymers are created by engineering the structure of the filaments with two components to provide structural reinforcement in the middle (core) while the outside polymer (shell) is selected to allow for enhanced diffusion. When the outside polymer has a significantly lower glass transition temperature (T_g) than the interior, the printed part can be post-process annealed at high temperatures to promote the welding of the interface without loss in the dimensional accuracy.[44] Other thermal post-processing methods can increase the mechanical properties of the printed parts; in particular, constrained remelting where the printed part is encased in salt can significantly improve the mechanical properties through re-solidifcation.[47-49] However, thermal annealing is not always effective for improving properties[50] and the constrained remelting method requires salt to be densely packed around the part to prevent distortions and then its removal to reveal the final part, which is time intensive. Solvent vapor annealing can improve the mechanical properties of high performance plastics,[51] but there are significant environmental, health, and safety concerns with solvent vapor processing. Finally, post-print heating (annealing) can sometimes increase the ultimate tensile strength of the part, but the efficacy is strongly dependent on the polymer.[52]

Interestingly, improvements in interlayer adhesion can be achieved through the addition of low molecular weight (M_w) PLA to commercial PLA filaments.[53] In this case, the low M_w

component acts to improve diffusion and increase the entanglements across the interfaces. However, high molecular weight polymers tend to be preferred for high performance due to the increased entanglement density. Engineering of the molecular weight distribution is commonly employed to balance processibility and mechanical performance in traditional plastic manufacturing; injection molding can utilize trimodal distributions of polymers to achieve this balance.[54] However, these approaches to engineer the molecular weight in filaments have not been extensively investigated as a route to enhance performance with MEAM.

Here, we systematically investigate how the molecular weight distribution impacts printability and the mechanical properties of the printed parts. Poly(methyl methacrylate) (PMMA) is used as a model polymer due to its availability with a variety of molecular weights and the prior use of PMMA as a base polymer for examining hydrogen bonding and nanoparticles to improve performance of 3D printed parts.[29,31,34,35] PMMA is more commonly used in 3D printing as a resin in vat photopolymerization than in MEAM, where PMMA resins are frequently utilized in dentistry.[55] In MEAM, we demonstrated that manipulating the average molecular weight through blending impacts performance and printability; too low of a weight average molecular weight (M_w) leads to brittle filaments that fracture in the pinch rollers, while too high of M_w leads to back flow and an inability to effectively print. However, the average M_w does not alone predict printability or performance. Blending low and high molecular weight PMMA to match the M_w of a base PMMA provides a route to systematically alter the molecular weight distribution (dispersity) without significantly impacting the average M_w. In this work, we show that molecular weight engineering, when guided by rheology, is an effective route to enhance the mechanical performance of 3D printed parts.

2. Results and Discussion

Four commercial PMMA samples with weight average molecular weights (M_w) of 38.4, 73.0, 78.3, and 309.1 kg mol^{-1}were used as polymers for understanding the effect of molecular weight distribution on 3D printed part properties. GPC traces for these polymers are shown in **Figure S1**. As the 78.3 kg mol^{-1} PMMA is similar to the molecular mass used in prior reports for 3D printing of PMMA, this polymer was used as the base for most of the studies to engineer the molecular weight distribution to provide facile comparisons with the literature.

2.1. Rheology and Printability of Blends

Rheology provides insight into polymer dynamics necessary for diffusion to create strong parts, but also the printability of the polymer by MEAM.[56] **Figure 1a** illustrates the viscosity of the four base PMMA polymers (M_w=38.4, 73.0, 78.3, and 309.1 kg mol^{-1} PMMA) at 240 °C as determined by capillary rheometry. These data are reported over the shear rate range ($\dot{\gamma}$ =100-4000 s^{-1}) typical for printing with MEAM.[57,58] PMMA exhibits shear-thinning behavior and the viscosity increases with increasing molecular weight. The rate dependence of the viscosity is described as a power law over the shear rates measured. The exponent decreases with M_w from n = 0.75 for the 38.4 kg mol^{-1} sample to n = 0.13 for the 309.1 kg mol^{-1} sample. For the lower M_w PMMA, dripping of the PMMA from the capillary occurred at the lower shear rates examined to prevent an accurate determination of the viscosity at these conditions.

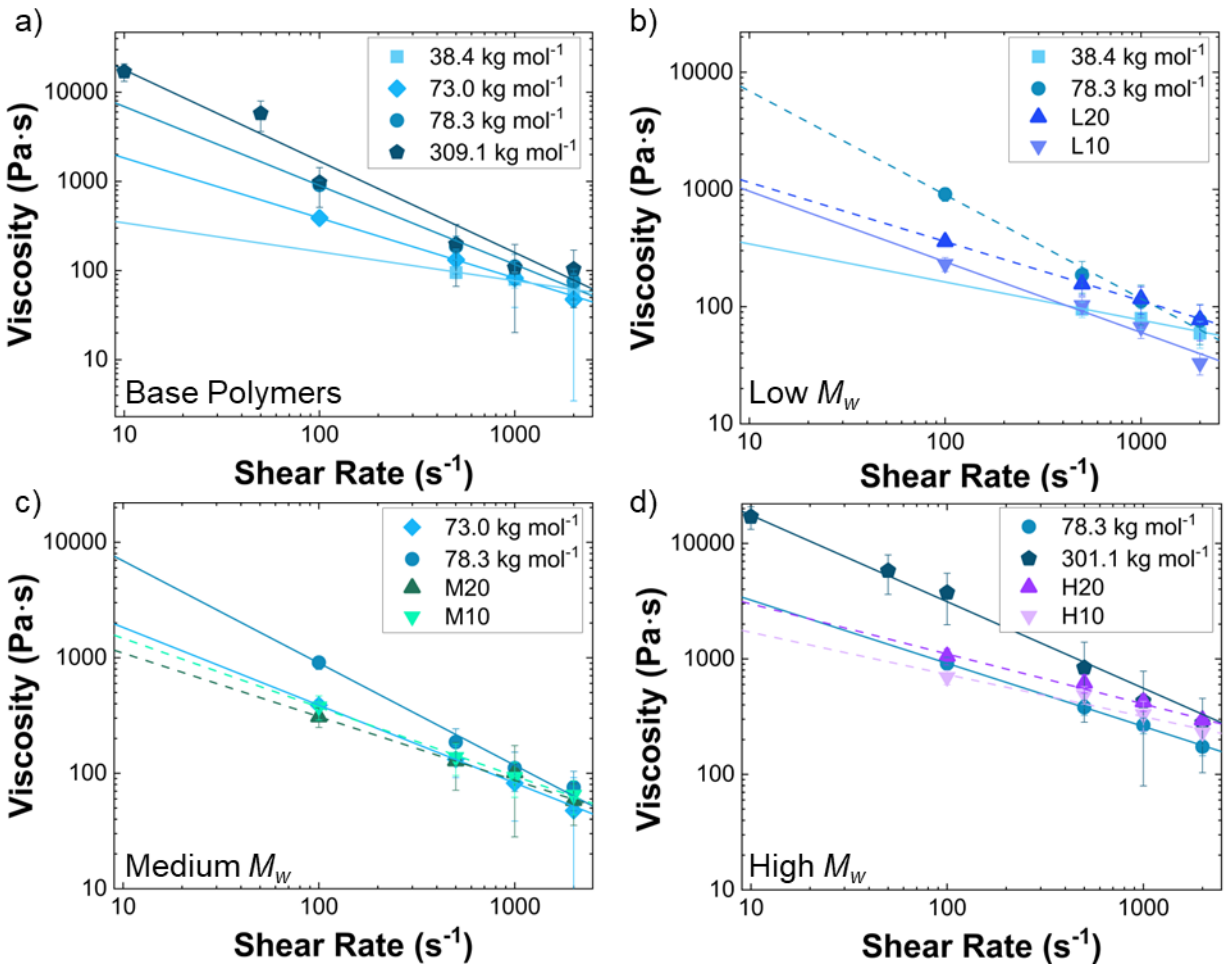

Figure 1. Shear viscosity at 240°C of **a)** base polymers and blends of **b)** low M_w (L10 and L20) with 78.3 kg mol^{-1} PMMA, **c)** medium M_w (M10 and M20) with 78.3 kg mol^{-1} PMMA, and **d)** high M_w (H10 and H20) with 78.3 kg mol^{-1} PMMA (see **Table 1**). The solid lines are the best fit of the viscosity of base polymers to a power law model and the dashed lines are the best fit of the blends to a power law model.

Table 1. Nomenclature, composition, M_w, and dispersity of polymer blends with low, medium, and high M_w PMMA in the base (78.3 kg mol^{-1}) PMMA

Name	Weight Percent[a]	M_w (kg mol^{-1}) [b]	$Đ$	Theoretical M_w (kg mol^{-1})	Zero-Shear Viscosity (η_0) (Pa s)
L20	20% 38.4 kg mol^{-1}	65.5	3.07	70.3	$2.44 \cdot 10^5 \pm 1.87 \cdot 10^4$
L10	10% 38.4 kg mol^{-1}	71.2	2.59	74.3	$6.35 \cdot 10^5 \pm 9.34 \cdot 10^4$
M20	20% 70.3 kg mol^{-1}	79.6	1.88	77.2	$2.71 \cdot 10^5 \pm 9.34 \cdot 10^4$
M10	10% 70.3 kg mol^{-1}	71.2	2.63	77.8	$3.44 \cdot 10^5 \pm 3.05 \cdot 10^4$
H20	20% 309.1 kg mol^{-1}	131.7	1.97	124.5	$8.30 \cdot 10^5 \pm 7.99 \cdot 10^4$
H10	10% 309.1 kg mol^{-1}	87.4	2.72	101.4	

[a] remainder of the blend composition is 78.3 kg mol^{-1} PMMA.
[b] as determined by GPC

To determine the sensitivity of the shear viscosity to M_w, 78.3 kg mol^{-1} PMMA was mixed with 38.4 kg mol^{-1}, 73.0 kg mol^{-1}, and 309.1 kg mol^{-1} PMMA at the compositions shown in **Table 1**. Number average molecular weight and *Z*-average molecular weight (M_n and M_z) for all polymers and polymer blends can be found in **Table S1**. The M_w and dispersity ($Đ$) reported in **Table 1** was determined by Gel Permeation Chromatography (GPC) with traces for the blends shown in **Figure S2**. These measured M_w tend to be lower than expected from the blend composition and the known M_w for the components. This may be due to some reduction in M_w during the compounding. However, there are a couple of cases where the measured M_w is measured to be greater than theoretically expected. As these blends contain a minority of the added PMMA, the statistics of sampling can be important for the GPC traces especially with the small amount of the PMMA examined. The differences between the measured and known M_w are likely associated with sampling based on the variances being both high and low from the theoretical value.

Blends of 10 wt.% and 20 wt.% 38.4 kg mol^{-1} in 78.3 kg mol^{-1} PMMA (L10 and L20, respectively) did not lead to a significant reduction in shear viscosity in comparison to the base PMMA (see **Figure 1b**). This insensitivity of shear viscosity to composition would suggest that diffusion is not significantly impacted by the inclusion of the lower M_w component as diffusion is inversely correlated with viscosity. However, the diffusion occurs at essentially zero shear rate after the road has been printed, relying primarily on polymer flexibility and mobility.[56,59] Zero-shear viscosity (η_0) was extrapolated from small amplitude oscillatory shear (SAOS) data using the Carreau-Yasuda model and time-temperature superposition based on the Williams-Landel-Ferry (WLF) equation. This calculation assumed the equivalence of the complex viscosity to the steady-state viscosity via the Cox-Merz rule.[60] **Figure S6** illustrates the larger deviation in viscosity at low shear rates for L10 and L20 than at high shear rates. This combination of differences in the zero-shear viscosity and essentially invariant viscosity at

shear rates associated with printing suggests that the printability of the filaments is not impacted by the low M_w component, but diffusion should be enhanced during weld formation because of the lower zero-shear viscosity. Intriguingly, there is a clear decrease in viscosity with the addition of 20 wt.% 73.0 kg mol^{-1} in 78.3 kg mol^{-1} PMMA (M20) as shown in **Figure 1c**, but no apparent change in viscosity for M10. The increased sensitivity of the viscosity at high shear rates to the middle M_w PMMA (M20) compared to the low M_w PMMA (L20) is counter to expectations based on the molecular weights, but the pure 73.0 kg mol^{-1} PMMA exhibits a lower viscosity than the 38.4 kg mol^{-1} PMMA at 200 °C (see **Figure S4**). The 73.0 kg mol^{-1} PMMA is sourced from a different supplier, so these differences in viscosity may be related to changes in the relative dyads in the tacticity of the atactic PMMA.[61] Blending the high M_w PMMA into the base 78.3 kg mol^{-1} PMMA increases the viscosity at high shear rates slightly for H10 and H20 in **Figure 1d**, but not outside the uncertainty of the measurement. However, the zero-shear viscosity is significantly impacted by the changes to the molecular weight distribution as shown in **Figure S6**. The similarity in the viscosity at shear rates associated with filament extrusion and printing for most of the PMMA samples examined should enable common conditions to produce the filaments as well as direct comparisons for the printing.

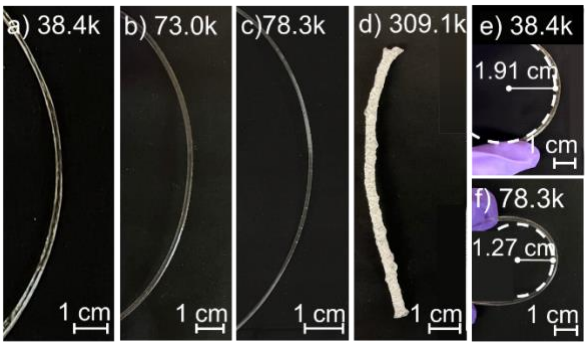

Figure 2. Photographs of PMMA filaments of **a)** 38.4 kg mol^{-1} PMMA, **b)** 73.0 kg mol^{-1} PMMA, **c)** 78.3 kg mol^{-1} PMMA, and **d)** 309.1 kg mol^{-1} PMMA. The maximum curvature obtainable prior to failure for the filaments depends on the molecular weight; the largest curvature is shown for **e)** the 38.4 kg mol^{-1} PMMA and **f)** the 78.3 kg mol^{-1} PMMA from the last frame in a video before failure of the filament. The radius of curvature prior to failure is listed in the panels.

Production of filaments from the base polymers provides some insights into the printability of these polymers. **Figure 2** illustrates the visual appearance of the filament for the different molecular mass PMMA. **Figure 2a-2c** illustrate the clear 38.4 kg mol^{-1} PMMA,73.0 kg mol^{-1} PMMA, and 78.3 kg mol^{-1} PMMA filaments, which are uniform with diameter of d = 1.79 ± 0.05, d = 1.79 ± 0.04 mm and d = 1.71 ± 0.02 mm, respectively. The appearance of the high M_w sample (309.1 kg mol^{-1}) differs from the others (**Figure 2d**); it is opaque white in appearance (from light scattering), the surface is not smooth, and the non-uniformity of the filament renders it unprintable. The diameter (d = 5.17 ± 0.92 mm) is much larger due to increased die swell for high M_w (309.1 kg mol^{-1})[62] and the surface of the filament exhibits features consistent with melt fracture.[63] In addition to the uniformity of the diameter, the flexural strength of the filament is important for printability. Bending the 38.4 kg mol^{-1} PMMA filament leads to catastrophic failure at larger radius of curvature than the 78.3 kg mol^{-1} as shown in **Figure 2e** and **2d**. The images of the bent filaments shown are the last frame of a video before the catastrophic failure of the filament as the filaments are bent. Videos illustrating the bending and failure of the filaments are included as Supplementary Information. This brittleness of the 38.4 kg mol^{-1} PMMA filament leads to printability issues as the small stresses exerted by the pinch rollers in the 3D printer are sufficient to crush the filament into powder. Although the molecular mass is approximately 3 times the entanglement molecular mass (M_e = 9.8 kg mol^{-1}) for PMMA, the number of entanglements is insufficient to prevent failure at low strains,[64] including under compression.[65] PMMA is brittle for viscosity average molecular weight (M_v) less than 25 kg mol^{-1} (2.5 entanglements per chain) and PMMA become ductile at approximately 60 kg mol^{-1}, or ~ 6 entanglements per chain.[66] Increasing the number of entanglements per chain increases flexibility, so the filaments can be bent without breaking as shown in **Figure 2f** for the 78.3 kg mol^{-1} PMMA. The smallest radius of curvature for the 38.4 kg mol^{-1} sample was 50% greater than that of the 78.3 kg mol^{-1} sample (1.91 cm as compared to 1.27 cm) to illustrate the significant change in brittleness on increasing M_w. When considering the blends, the following

potential challenges can be predicted: high concentrations of 38.4 kg mol^{-1} PMMA will embrittle the filament. For L20, the filament tended to break during printing in the pinch rollers to inhibit the ability to produce specimens. Second, the filament uniformity of the blends with 309.1 kg mol^{-1} PMMA could be problematic. Although uniform filaments could be produced with H10 and H20, neither could be properly extruded during printing at 240 °C due to back flow as will be described later.

The first series of blends, whose rheological properties are described in **Figure 1,** have varying average molecular mass, so changes in viscosity can be readily attributed to the M_w, but this challenges the understanding of how the molecular mass distribution itself impacts the printability. To address if altering the molecular mass distribution without changing the average M_w can impact printability and performance, ternary blends of PMMA were examined as shown in **Table 2** that alter the molecular mass distribution without impacting the average M_w. A blend of the 38.4 kg mol^{-1} (85.5 wt.%) and 309.1 kg mol^{-1} (14.5 wt.%) PMMA was mixed to a target M_w of 78 kg mol^{-1}, then melt-compounded with the pure 78.3 kg mol^{-1} PMMA to attempt to produce a constant average M_w with different distributions.

Table 2. Nomenclature, molecular weight, and dispersity of PMMA made with a 171:29 blend of 38.4 and 309.1 kg mol^{-1} melt mixed with 78.3 kg mol^{-1} PMMA, all with a targeted average M_w of 78.3 kg mol^{-1}.

Name	Weight Percent[a]	M_w (kg mol^{-1}) [b]	$Đ$	Theoretical M_w (kg mol^{-1})	Zero-Shear Viscosity (η_0) (Pa s)
B100	100% blend	51.7	3.68	78.3	$8.28 \cdot 10^5 \pm 3.04 \cdot 10^4$
B50	50% blend	75.5	3.27	78.3	$3.93 \cdot 10^5 \pm 4.78 \cdot 10^4$
B20	20% blend	70.2	2.37	78.3	$4.32 \cdot 10^5 \pm 5.00 \cdot 10^4$
B10	10% blend	71.9	2.24	78.3	$4.33 \cdot 10^5 \pm 5.01 \cdot 10^4$

[a] remainder of the blend composition is 78.3 kg mol^{-1} PMMA.
[b] as determined by GPC

Although the target M_w is constant, measurements of the blends by GPC demonstrated a reduction in the average M_w for the mixtures (**Table 2**). GPC traces for these blends can be found in **Figure S2b**. This reduction is greatest for the blend with the largest high molecular

weight content and this reduction in M_w is attributed to chain scission from high shear environment in the compounding and the presence of the high molecular mass PMMA as chain scission probability in extrusion increases with increasing molecular mass. Despite exhibiting the highest and lowest average M_w of these blends, B100 and B50 exhibit lower viscosity than the base 78.3 kg mol^{-1} PMMA at the high shear rates associated with printing (see **Figure 3**). B100 and B50 have a high content of 38.4 kg mol^{-1} PMMA, which may lead to reduced viscosity. Nonetheless, both B100 and B50 were too brittle to print. B10 and B20 exhibit viscosities that are statistically similar to the base 78.3 kg mol^{-1} PMMA and thus provide a route to examine the impact of the trimodal distribution of M_w on the printed properties without impacting the printing process itself which is generally controlled by the filament rheology.[56]

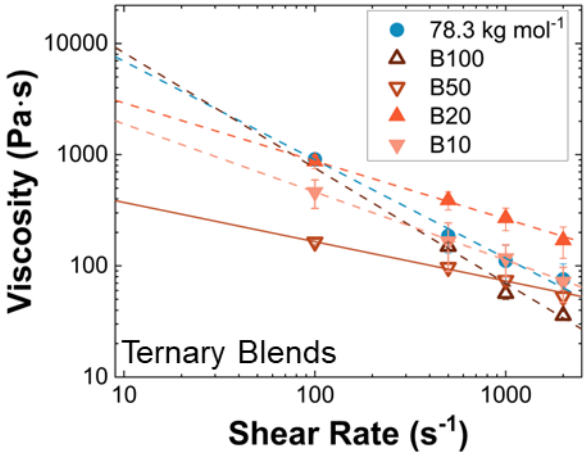

Figure 3. Shear viscosity of 78.3 kg mol^{-1} PMMA and the ternary blends of B10, B20, B50, and B100 (see **Table 2** for compositional information**)** at 240 °C from capillary rheometry. The lines are the best fits to a power law model.

Being able to *a priori* determine printability of a polymer is highly desired to avoid challenges in printing and potential equipment damage from back flow or shards of broken filament. One approach that has been recently proposed is the Flow Identification Number (FIN), which provides a cutoff for printability without back flow.[67]

$$FIN = \frac{\Delta P/L}{\eta \cdot v} \cdot \pi (D_B^2 - D_F^2) \quad (1)$$

Here, $\Delta P/L$ is the pressure gradient inside the hot end of the printer (L = length), η is viscosity, v is feed rate, D_B (= 0.4 mm) is the diameter of the hot end, and D_F is the filament diameter.[67] Pressure drop (ΔP) was determined using the Bellini model.[68,69] All other values calculated from the 0.4 mm hot end used in printing. Prior work identified three regimes: printable (FIN < 153), transition (153 < FIN < 185), and back flow (FIN > 185).[67] To test if this approach applied to the PMMA blends here, the FIN was calculated from the viscosity at $\dot{\gamma} = 500\ s^{-1}$ to determine which blends were predicted to be printable.

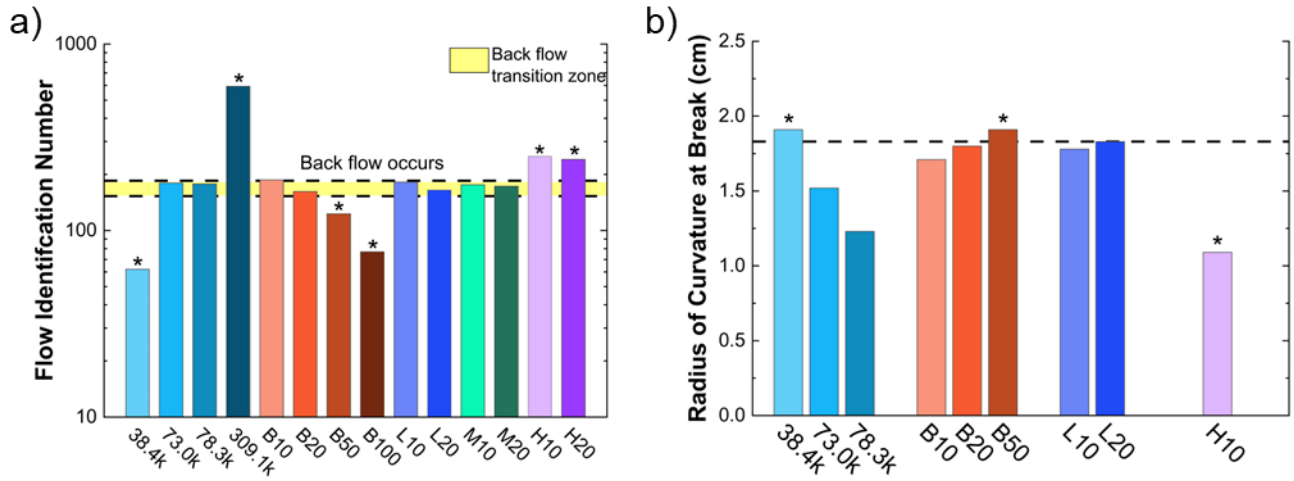

Figure 4. a) Flow identification number (FIN) for base polymers and blends at 240 °C. The yellow shaded region indicates the transition zone where back flow may occur (153 < FIN < 185), higher FIN results in back flow. **b)** Radius of curvature of filaments at failure determined from video frames. The dotted line indicates the radius (1.83 cm) above which the filaments are too brittle to print. The stars indicate samples that were not printable in this work.

Figure 4a shows the FIN for each PMMA composition that was extruded into filaments. The shaded area represents the transition zone with the high cut-off of FIN = 185, above which back flow is predicted. Indeed, back flow was observed in the initial print trials of the high M_w polymer blends H20 and H10 and this back flow inhibited the printing of high-quality parts. The three PMMA samples with FIN > 185 all suffered from the back flow, while all samples within the transition region were printable. Interestingly, the three samples with low FIN numbers outside of the transition region were not able to be printed due to the samples being

too brittle. To address this point, the radius of curvature at failure for the different PMMA compositions was examined through simple bending of the filaments as shown in **Figure 2 and Figure S8**. The filament diameter was consistently at 1.79 ± 0.04 mm, irrespective of blend composition. Filaments with a radius of curvature greater than 1.9 cm were found always too brittle to print, which may help to inform about requirements for the toughness of the filaments to be printable as shown in **Figure 4b**. With the printing of the L20, the filament sometimes failed due to brittleness and thus this sample likely represents a transition from too brittle to printable: the minimum radius of curvature of the L20 was 1.83 cm as additional bending led to catastrophic fracture of the filament. As the radius of curvature at break is directly related to the flexural modulus of the polymer, this method of determining printability of polymers should be translatable to understanding the printability of other polymers. However, the origins of the lower limit of the curvature for printability appears to be associated with the pressure exerted by the pinch rollers as the failure tends to occur within the rollers during print trials. As the geometry of the filament feed and pressure imposed by the pinch rollers will be dependent on the exact MEAM printers, the limit of curvature for printability is likely quantitatively slightly different in other systems due to the printer. However, we would expect that a qualitatively similar curvature limit for other polymers that could be used for determining printability of custom materials. This assessment of printability through curvature is useful for brittle materials. In our quick assessment of a variety of commercially available filaments including ABS, PC/ABS, PEEK, ULTEM®, the radius of curvature for these 1.75 mm filaments is significantly less than the 1.83 cm found to be the limit for printability of the PMMA. This suggests that the bending measurement to assess printability should be directly applicable to other polymer systems for MEAM.

2.2 Mechanical Testing of 3D Printed PMMA

The described filaments were printed directly into Type V (ASTM D638) dog bones for tensile testing. The specimens printed with a raster angle of 0°, which is defined relative to the direction of tensile deformation during mechanical testing, essentially examine the strength of the printed roads. The load bearing of these specimens during tensile deformation does not require high quality welds between printed roads. This is counter to those printed with a 90° raster angle where only the outside border is continuous between the grips for the tensile test. For the specimens printed with 90° raster angle, the sample essentially consists of welds, which typically results in much inferior mechanical properties. In examination of **Figure 5a**, there is generally limited differences between the two raster angles for the different PMMA samples. This raster angle invariance is indicative of well-developed welds in the 90° samples under the print processing conditions examined.

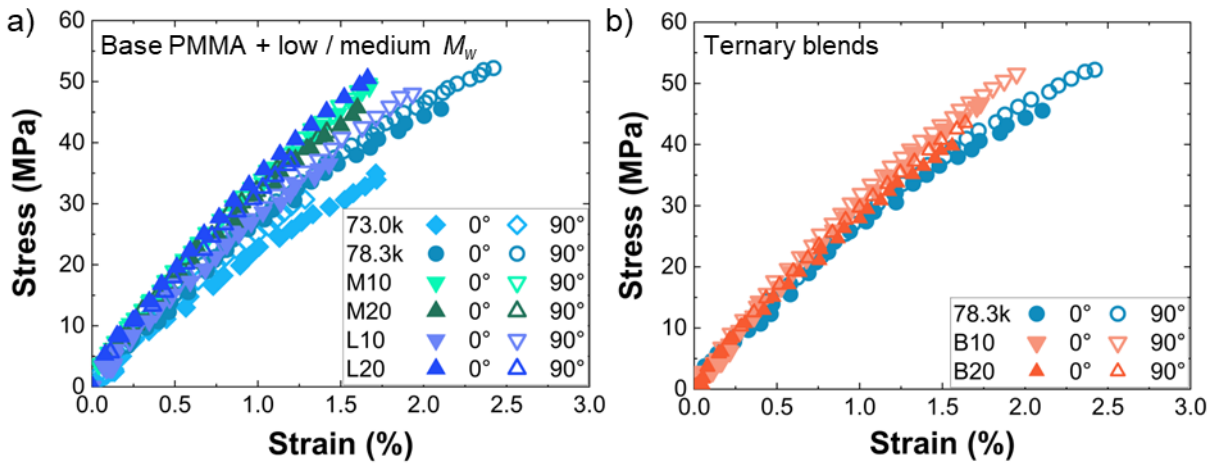

Figure 5. Representative stress-strain curves from ASTM D638 Type V dog bones for **a)** base polymers: 73.0 kg mol^{-1} and 78.3 kg mol^{-1} as well as blends with medium and low M_w (M10, M20, L10, and L20) PMMA; and **b)** ternary blend (B10 and B20). Open symbols indicate a raster angle 90° to the direction of tensile testing, closed symbols indicate a raster angle 0° to the direction of tensile testing.

In comparing the engineered blends with bimodal M_w distributions to the base PMMA samples, **Figure 5a** illustrates generally an increase in the stiffness of samples printed with the blends. Despite the intermediate average M_w for the samples tested (**Table 1**), the 78.3 kg mol^{-1} PMMA led to the lowest Young's modulus samples (E = 2.24 ± 0.15 GPa and 2.10 ± 0.07 GPa for a 0°

and 90° raster angle, respectively). The addition of up to 20 wt.% of the low M_w PMMA (38.4 kg mol^{-1}) still enabled printability of the filaments, although approximately 50% of the print starts ended in failure due to the brittleness of the L20. The Young's modulus of the printed PMMA increased with the blends, as shown in **Figure 5a**. The Young's modulus of the 78.3 kg mol^{-1} PMMA printed at 0° is E(78.3 kg mol^{-1}) = 2.24 ± 0.15 GPa and this modulus is marginally increased with L10 to E(L10)= 2.46 ± 0.10 GPa.

Despite reduction in the molecular weight and challenges with printability due to the brittle filaments, the Young's modulus of L20 is substantially increased to E(L20) = 2.98 ± 0.11 GPa. This increase is greater than obtained with either M10 and M20, which have Young's moduli of E(M10) = 2.62 ± 0.13 GPa and E(M20) = 2.71 ± 0.21 GPa, respectively. The best performance with the lower M_w blend indicates that the improvements in the mechanical properties are likely associated with increased diffusion that will impact both entanglements across the printed interfaces as well as the relaxation of the chain alignment that occurs during the printing process. Interestingly, the correlation between zero-shear viscosity and Young's modulus and UTS depends on the raster angle of the printed part (see **Figure S9**). For specimens with a 0° raster angle, both Young's moduli and UTS decrease as η_0 increases. However, for the 90° raster angle, which relies on the diffusion of the polymers across the interfaces for strength, there is no statistically significant trend for the Young's moduli with η_0, but the UTS appears to increase as η_0 increases. This is counter to expectations as diffusion is inversely correlated with η_0 and improvements in diffusion were expected to be the controlling factor for improvements in mechanical performance with the blends. Alternatively, the characteristic time can be determined from Generalized Newtonian Fluid (GNF) models, which provides a time constant that describes relaxation of the polymer.[70] As Carreau-Yasuda is a GNF, the fits can also extract the characteristic time (λ) as a function of the blend composition. **Figure S10** illustrates that the correlation between the characteristic time (λ) and mechanical properties is not significantly better than the prior examination of zero shear viscosity. This points towards

a more complex relationship between rheology and the tensile properties of the printed part that likely depends strongly on the thermal history.

One route to address the brittleness of the blends with high performance is to include some small amount of higher molecular weight component that provides a high number of entanglements per chain to toughen the material. This was accomplished with ternary PMMA blends (**Table 2**) that theoretically had the same M_w. Changes to the M_w distribution can also improve the stiffness of the printed PMMA as shown in **Figure 5b**. The addition of the 309.1 kg mol^{-1} PMMA lead to an increased strain at break (ε_b) in comparison to the L10 and L20. However, for all blends the strain at break was decreased in comparison to the base 78.3 kg mol^{-1} PMMA. The Young's moduli of B10 and B20 are approaching, or comparable to, the lower end of the reported Young's modulus of traditionally manufactured PMMA,[71] which indicates the potential for improving the mechanical properties of 3D printing parts through engineering of the molecular weight distribution.

Figure 6a summarizes the impact of the different blends on the Young's modulus of the printed parts. The binary blends provide improvements in the Young's moduli, but the blend to achieve the highest Young's modulus is also the most brittle (L20). The trimodal molecular weight distributions for B10 and B20 led to similar increases in the modulus to L20. For the trimodal blends, the addition of low M_w PMMA increase diffusion, but increased brittleness was observed as manifested by a decrease in the strain at break (see **Figure 6b)**. Even with the addition of the high M_w component, the strain at break with B20 is significantly reduced due to the large low M_w content. The strain at break did not always simply trend with M_w as ε_b(L10) = 1.95 ± 0.11% is marginally greater than that for the ε_b(M10) = 1.73 ± 0.09%. In all cases, the 3D printed materials fail at significantly lower strains than typically reported for PMMA with more traditional plastic processing.[72] As shown in **Figure 6c**, the average ultimate tensile strength (σ_{UTS}) was modestly increased (approximately 10%) for the M10, but there was significant variability with the M20, L10 and L20 blends at different raster angles. The UTS

for the printed parts appears to limited to approximately σ_{UTS} = 50 MPa irrespective of the blend composition, which is lower than the typical reported values for PMMA with traditional processing.[73] The molecular weight engineering strategy provides a route to produce 3D printed PMMA with Young's moduli at the lower end of reported values for traditionally manufactured PMMA (see **Figure 6a**).[71] The improvements in Young's moduli does come at the expense of the ductility of the 3D printed samples.

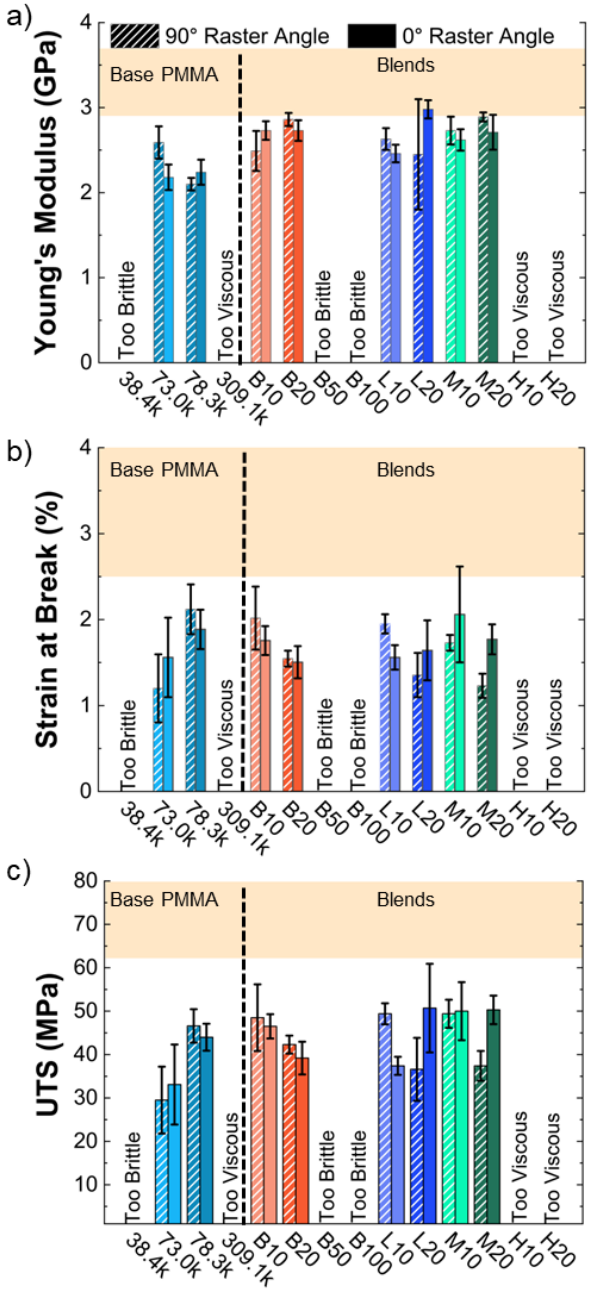

Figure 6. Summary of the **a)** Young's modulus, **b)** strain at break, and **c)** ultimate tensile strength (UTS) for the printed PMMA samples with different molecular weight distributions.

Data for both 90° (hatched) and 0° (solid) raster angles are presented. The shaded regions across each of the plots indicate the range for literature reported values for injection molded PMMA.

2.3 Comparison to Previous Approaches to the Improvements in Mechanical Properties of 3D Printed PMMA

A variety of methods to address the mechanical properties of MEAM PMMA have been reported in the literature.[23,24,29,31,34,35,52,74] Many of these have examined samples printed with a crosshatch raster infill associated with 45° raster angles.[29,31,34,35] **Figure 7** shows the stress-strain curve for B10 printed with a -45°/+45° crosshatch raster infill; B10 was one of the better performing blends at both 0° and 90° raster angles. The initial slope associated with the Young's modulus is higher with B10 in comparison to the 78.3 kg mol^{-1} PMMA printed at 0° or 90° raster angles. This indicates similar qualitative improvements with the blend using a crosshatch infill. These results provide a route for a more direct comparison to some of the previously reported printing strategies to improve the mechanical properties of PMMA.

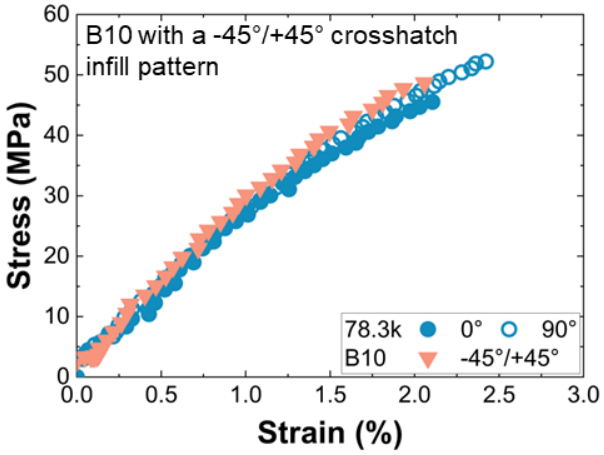

Figure 7. Stress-strain curve for B10 samples in a cross-hatching (-45° / +45°) infill pattern with comparison to the 78.3 kg mol^{-1} PMMA at 0° and 90°. Open circles indicate a raster angle 90° to the direction of tensile testing, closed circles indicate a raster angle 0° to the direction of tensile testing. The +45°/-45° raster angle is indicated by an upside-down triangle.

Table 3 summarizes a variety of different methods that have been used to increase the mechanical properties of 3D printed PMMA. As print parameters and the molecular weight distribution impact the quantitative values for the mechanical properties, **Table 3** includes information about the control sample, labeled base case, for a comparison. The base case for the results reported here is the 78.3 kg mol^{-1} PMMA. It should be noted that even the base case here produces parts with higher Young's moduli than several of the methods reported in the literature, which can be attributed to the printer and the use of a higher temperature for the print bed than several of the studies. Using the trimodal M_w distribution led to higher Young's moduli than obtained with other methods except for the short glass fibers (SGFs) composites that were aligned in the direction of the tensile stress.[74] Higher UTS was again possible with composites,[31,74] but the best performing blend in this work led to comparable UTS to the best case with other methods (see **Table 3**). Moreover, the routes to achieve better performance tend to rely on inorganic fillers that will impact the rheology to make clogging more problematic and increase the wear to the hot end. As a result, there may be advantages to being able to maintain an all-polymeric system with the engineering of the molecular weight distribution. These results illustrate that engineering of the molecular weight distribution of the base polymer used for filaments in 3D printing offers the potential to improve the mechanical properties to extents similar or exceeding other more synthetically and compositionally complex methods. This relatively simple approach to engineering the molecular weight distribution through melt compounding offers the potential to enhance the performance of filaments for MEAM without added costs associated with new synthetic polymers or small fillers that can cause clogging in the hot end of 3D printers.

Table 3. Alternative methods to increase Young's modulus and UTS of MEAM PMMA and corresponding mechanical properties, the best sample from the paper is reported.

Method	Tensile bar size[a]	Raster Angle	M_w (kg mol^{-1})	Case	Young's Modulus (GPa)	UTS (MPa)	Strain at break (%)	Ref

Altering porosity (air gap)	Type V	0°/90°	unspecified	Base	0.16	7	unspecified	23
				Best	0.25	11.8	unspecified	
Addition of silica nanoparticles	Type V	+45°/-45°	100	Base	1.223 ± 0.159	18 ± 3	2.3±0.9	34
				Best	2.163 ± 0.99	42 ± 4	4.4 ± 0.6	
Addition of a hydrogen bonding copolymer	Type V	+45°/-45°	65	Base	1.493 ± 0.065	21 ± 6	2.4 ± 1.0	29
				Best	2.240 ± 0.066	42 ± 5	2.3 ± 0.7	
Post-print heat treatment 90% of T_g	Type V	unspecified	unspecified	Base	unspecified	60	4.5	52
				Best	unspecified	80	5.5	
Addition of polymer-grafted nanoparticles (PGNPs)	Type V	+45°/-45°	100	Base	1.220 ± 0.160	18 ± 3	2.3 ± 0.9	35
				Best	1.990 ± 0.130	39 ± 5	3.1 ± 0.7	
Addition of PGNPs with hydrogen bonding grafted chains	Type V	+45°/-45°	72	Base	1.223 ± 0.158	21 ± 6	2.3 ± 0.9	31
				Best	2.322 ± 0.98	52 ± 3	2.3 ± 0.3	
Addition of short glass fibers	Type I	0°	unspecified	Base	3.3	40	unspecified	74
				Best	4.55	74	unspecified	
Altering infill, raster angle, print speed	Type V	22.5°	unspecified	Base	0.024 ± 0.004	6.53 ± 0.83	unspecified	24
				Best	0.224 ± 0.001	44.23 ± 0.47	unspecified	
Trimodal distribution of M_w	Type V	0°	78.3	Base	2.24 ± 0.15	44.0 ± 3.1	1.88 ± 0.23	This work
		90°	78.3	Base	2.10 ± 0.07	46.6 ± 3.8	2.12 ± 0.29	
		90°	65.5	L20	2.98 ± 0.11	50.7 ± 10.2	1.64 ± 0.35	
		90°	70.2	B20	2.86 ± 0.77	42.3 ± 2.1	1.55 ± 0.09	
		+45°/-45°	71.9	B10	2.78 ± 0.051	40.5 ± 7.3	1.48 ± 0.32	

[a]ASTM D638

3. Conclusion

Increasing the mechanical properties of MEAM parts, without adding expensive fillers or complex and costly post-processing techniques, is important to further expand the capabilities of MEAM towards new applications. In this work, we investigated the effect of M_w and its distribution on Young's modulus, ultimate tensile strength, and strain at break for 3D printed PMMA by melt-compounding a low, medium, and high M_w polymer with a base polymer of 78.3 kg mol^{-1}. We have shown that the addition of a low molecular weight polymer to the filament can increase the Young's modulus of the part. The polymer blends containing high M_w PMMA were too viscous to successfully print due to back flow in the print nozzle. A trimodal molecular weight distribution with a targeted identical M_w as a base polymer allowed for

increased Young's modulus compared to the base polymer with a smaller negative impact on polymer ductility than with the addition of low M_w PMMA alone. Finally, we were able to use the radius of curvature of the PMMA filaments to predict if they will be too brittle to print ($r >$ 1.83 cm). The mechanical properties of the PMMA with engineered M_w distributions tended to outperform several complex strategies including nanoparticles and multiple hydrogen bonds. The molecular weight distribution appears to be a simple handle to provide enhancements in the performance for MEAM.

4. Experimental Section

4.1 Materials

Poly(methyl methacrylate) (PMMA) (nominal M_w = 35 kg mol^{-1}, 75 kg mol^{-1}, and 540 kg mol^{-1}) was purchased from Scientific Polymer Products (SP^2, Ontario, NY, lot numbers: 120610029, 510624028, 010908024, respectively). PMMA (nominal M_w = 100 kg mol^{-1}) was received from PolySciences, Inc (Washington, PA, lot number A825610). Pentaerythritol tetrakis(3,5-di-tert-butyl-4-hydroxyhydrocinnamate) (98%) was obtained from Sigma-Aldrich (Taiwan). Prior to use, all polymers were dried at 100°C under vacuum for 24 hours. PMMA was dissolved in tetrahydrofuran (1 mg mL^{-1}) and characterized using gel permeation chromatography (GPC) on a TOSOH EcoSEC HCL-8320 GPC system with a refractive index detector. **Figure S1** illustrates the GPC traces for the four base PMMA samples in this study. **Table 4** summarizes the molecular weight characteristics of the base PMMA samples as determined from GPC. Polymers are referred to by their experimentally determined M_w.

Table 4. Molecular weights, zero-shear viscosity, and dispersity of base PMMA samples.

Nominal M_w (kg mol^{-1})	M_n (kg mol^{-1})	M_w (kg mol^{-1})	M_z (kg mol^{-1})	$Đ$	Zero-Shear Viscosity (η_0)
35	23.9	38.4	55.1	1.61	$3.13 \cdot 10^4 \pm 6.63 \cdot 10^2$
75	53.8	78.3	110.9	1.46	$6.74 \cdot 10^5 \pm 9.69 \cdot 10^4$
100	40.5	73.0	116.4	1.80	$1.68 \cdot 10^5 \pm 1.47 \cdot 10^4$

540	101.1	309.1	572.9	3.057	$1.12 \cdot 10^6 \pm 2.02 \cdot 10^5$

4.2 Compounding and Filament Fabrication

Blends of PMMA were compounded using a twin-screw extruder (HAKKE MiniLab 3 Micro Compounder) at 220°C and 100 rpm. All the blends contained 0.2 wt.% of pentaerythritol tetrakis(3,5-di-tert-butyl-4-hydroxyhydrocinnamate) to minimize oxidation during processing. Two series of blends were examined with the base polymer for all the blends being 78.3 kg mol^{-1} PMMA. To probe the effect of the average molecular weight, 10 wt.% or 20 wt.% of either M_w = 38.4, 73.0, and 309.1 kg mol^{-1} PMMA were added to the 78.3 kg mol^{-1} PMMA. To address the impact of the molecular weight distribution, a mixture of 88.7 wt.% 38.4 kg mol^{-1} and 11.3 wt.% 309.1 kg mol^{-1} PMMA was used to maintain a constant M_w of 78 kg mol^{-1} (actual M_w for nominal 75 kg mol^{-1} PMMA) and blended with the 78.3 kg mol^{-1} at 10, 20, and 50%. Following melt-compounding, the PMMA blends were characterized by GPC with the results shown in **Table S1**. The high shear environment for the compounding leads to a reduction in the molecular weight for the blends.

Filaments of the base PMMA and the blends were produced using a capillary rheometer with a 3 mm diameter die. The filaments were extruded at 200°C with the piston moving at 40mm/min. The extrudate was collected onto spools (7.5 cm diameter) using a take up wheel (Bodine Electric Gear Motor powered by Dart Controls Digital DC Speed Control) at 10 rpm to draw the filament diameters down to 1.79 ± 0.04 mm, as shown in **Figure S3**. Individual filament diameters can be found in **Table S2**.

The bending of the filaments was performed by hand by slowing bending the filament until it broke. The bending process was recorded on video (iPhone) until failure occurred. The minimum radius of curvature was determined for all filaments (average diameter 1.79 ± 0.04 mm) from the video file. The last frame from the video prior to failure of the filament was

used to determine the minimum radius of curvature. The radius of curvature was determined from image analysis and fitting the inner radius of the bent filament to a circle.

4.3 3D Printing

Prior to printing, the filaments were dried for 16 h at 95°C using Roboze Plus Pro HT dryer. The dried filaments were printed using a Roboze One + Xtreme (Roboze, Apulia, Italy) at 240 °C using a 0.40 mm nozzle. The g-code for type V tensile bars (ASTM D638) was generated in Simplify3D software. Two tensile bars were printed at either 0° or 90° raster angle and 100% infill. A constant layer height (0.25 mm), print speed (1200 mm min^{-1}), and build orientation (XY) were used for the fabrication of the specimens. Five tensile bars were printed for each specimen type (filament composition and raster angle) for statistical analysis of mechanical response. **Figure S11** through **S19** contain photographs of the tensile bars before and after tensile testing.

4.4 Rheology

The flow properties of the base polymers and blends were determined. For direct comparison to the filament fabrication and printing conditions at comparable shear rates, the shear viscosity of the PMMA samples was determined at 200°C and 240°C using a single barrel capillary rheometer (Instron CEAST SR-20) with a 1.0 mm diameter die. **Figure S4** shows the shear viscosity data for the samples at 200°C. Measurements were performed at shear rates between 10 and 2000 s^{-1}. For each temperature, shear rate and composition, three different die lengths (5, 20, and 30 mm) were used. The viscosity was determined from the pressure and crosshead rate and corrected for end effects using two die lengths and the Bagley correction and the Weissenberg-Rabinowitsch correction. The rheological properties of the base polymers and blends were also assessed using small angle oscillatory shear (SAOS) measurements with a Discovery HR 20 rheometer (TA Instruments). Powdered samples were placed in between 25

mm diameter, stainless-steel parallel plates, heated it to 180°C, then compressed it to a 1000 μm gap once melted. The temperature was decreased to 130°C in 10°C increments. A frequency sweep from 0.1 to 100 Hz using a strain of 1.0% was done at each temperature. Time-temperature superposition analysis was done in the TRIOS software to construct a master curve with a 170°C reference temperature, via the Williams–Landel–Ferry (WLF) equation. This was used to determine zero-shear viscosity as well as storage modulus, loss modulus, and *tanδ*, as shown in **Figure S5.** Complex viscosity is plotted with a Carreau-Yasuda model fitting for each sample in **Figure S6.**

4.5 Mechanical testing

The printed type V tensile bars were tested at room temperature using conditions consistent with ASTM D638. The tensile tests were performed using an MTS Criterion Model 43 load frame with a 1 kN load cell. The cross head was controlled at 0.083 in min^{-1} (effective strain rate = 0.00138 s^{-1}) using TW Elite software. The true strain was determined using an MTS Advantage Video Extensometer with data collection at 10 Hz. Samples were pulled until failure.

Supporting Information
Supporting Information is available from the Wiley Online Library or from the author.

Acknowledgements

This work was partially supported by the National Science Foundation under grant no. CMMI-2011289. SFY acknowledges support through the SMART Scholarship, which is funded by OUSD/R&E (The Under Secretary of Defense-Research and Engineering), National Defense Education Program (NDEP) / BA-1, Basic Research. The authors acknowledge use of the Penn State Materials Characterization Lab for tensile measurements.

Received: ((will be filled in by the editorial staff))
Revised: ((will be filled in by the editorial staff))
Published online: ((will be filled in by the editorial staff))

References

[1] Valino, A. D.; Dizon, J. R. C.; Espera, A. H.; Chen, Q. Y.; Messman, J.; Advincula, R. C. *Prog. Polym. Sci.* **2019**, *98*, 101162.
[2] Tofail, S. A. M.; Koumoulos, E. P.; Bandyopadhyay, A.; Bose, S.; O'Donoghue, L.; Charitidis, C. *Mater. Today* **2018**, *21*, 22-37.
[3] Thomas-Seale, L. E. J.; Kirkman-Brown, J. C.; Attallah, M. M.; Espino, D. M.; Shepherd, D. E. T. *Int. J. Prod. Econ.* **2018**, *198*, 104-118.
[4] Pagac, M.; Hajnys, J.; Ma, Q. P.; Jancar, L.; Jansa, J.; Stefek, P.; Mesicek, J. *Polymers* **2021**, *13*, 598.
[5] Cano-Vicent, A.; Tambuwala, M. M.; Hassan, S. S.; Barh, D.; Aljabali, A. A. A.; Birkett, M.; Arjunan, A.; Serrano-Aroca, A. *Addit. Manuf.* **2021**, *47*, 102378.
[6] Jiang, Z.; Diggle, B.; Tan, M. L.; Viktorova, J.; Bennett, C. W.; Connal, L. A. *Adv. Sci.* **2020**, *7*, 2001379.
[7] Carolo, L. https://all3dp.com/2/fused-deposition-modeling-fdm-3d-printing-simply-explained/ (accessed July 30, 2023).
[8] Shahrubudin, N.; Lee, T. C.; Ramlan, R. *Procedia Manuf.* **2019**, *35*, 1286-1296.
[9] Spoerk, M.; Holzer, C.; Gonzalez-Gutierrez, J. *J. Appl. Polym. Sci* .**2020**, *137*, 48545.
[10] Gudadhe, A.; Bachhar, N.; Kumar, A.; Andrade, P.; Kumaraswamy, G. *ACS Appl. Polym. Mater.* **2019**, *1*, 3157-3164.
[11] Yang, C. C.; Tian, X. Y.; Li, D. C.; Cao, Y.; Zhao, F.; Shi, C. Q. *J. Mater. Process. Technol.* **2017**, *248*, 1-7.
[12] Mikula, K.; Skrzypczak, D.; Izydorczyk, G.; Warchol, J.; Moustakas, K.; Chojnacka, K.; Witek-Krowiak, A. *Environ. Sci. Pollut. Res.* **2021**, *28*, 12321-12333.
[13] Sanchez, F. A. C.; Boudaoud, H.; Camargo, M.; Pearce, J. M. *J. Cleaner Prod.* **2020**, *264*, 121602.
[14] Mohammed, M. I.; Wilson, D.; Gomez-Kervin, E.; Tang, B.; Wang, J. F. *ACS Sustainable Chem. Eng.* **2019**, *7*, 13955-13969.
[15] Peeters, B.; Kiratli, N.; Semeijn, J. *J. Cleaner Prod.* **2019**, *241*, 118313.
[16] El Magri, A.; El Mabrouk, K.; Vaudreuil, S.; Chibane, H.; Touhami, M. E. *J. Appl. Polym. Sci.* **2020**, *137*, 49087.
[17] Van de Voorde, B.; Katalagarianakis, A.; Huysman, S.; Toncheva, A.; Raquez, J. M.; Duretek, I.; Holzer, C.; Cardon, L.; Bernaerts, K. V.; Van Hemelrijck, D.; Pyl, L.; Van Vlierberghe, S. *Addit. Manuf.* **2022**, *50*, 102518.
[18] Bakir, A. A.; Atik, R.; Ozerinc, S. *J. Appl. Polym. Sci.* **2021**, *138*, 49709.
[19] Spoerk, M.; Savandaiah, C.; Arbeiter, F.; Sapkota, J.; Holzer, C. *Polym. Compos.* **2019**, *40*, 638-651.
[20] Kulkarni, P.; Marsan, A.; Dutta, D. *Rapid Prototyp. J.* **2000**, *6*, 18-35.
[21] Lambert, P. https://www.sculpteo.com/blog/2014/05/14/material-considerations-choose-right-plastic-production-method-part-2/ (accessed July 30, 2023).
[22] Shaffer, S.; Yang, K. J.; Vargas, J.; Di Prima, M. A.; Voit, W. *Polymer* **2014**, *55*, 5969-5979.
[23] Espalin, D.; Bourell, D.; Arcaute, K.; Rodriguez, D.; Medina, F.; Posner, M.; Wicker, R. *Rapid Prototyp. J.* **2010**, *16*, 164-173.
[24] Vidakis, N.; Petousis, M.; Mountakis, N.; Moutsopoulou, A.; Karapidakis, E. *Polymers* **2023**, *15*, 845.
[25] Abbott, A. C.; Tandon, G. P.; Bradford, R. L.; Koerner, H.; Baur, J. W. *Addit. Manuf.* **2018**, *19*, 29-38.
[26] Ai, J. R.; Vogt, B. D. *Prog. Addit. Manuf.* **2022**, 1009-1021.
[27] Guessasma, S.; Belhabib, S.; Nouri, H. *Polymer* **2015**, *81*, 29-36.
[28] Costanzo, A.; Cavallo, D.; McIlroy, C. *Addit. Manuf.* **2022**, *49*, 102474.

[29] Street, D. P.; Ledford, W. K.; Allison, A. A.; Patterson, S.; Pickel, D. L.; Lokitz, B. S.; Messman, J. M.; Kilbey, S. M. *Macromolecules* **2019**, *52*, 5574-5582.
[30] Niu, W.; Zhang, Z.; Chen, Q.; Cao, P.-F.; Advincula, R. C. *ACS Mater. Lett* .**2021**, *3*, 1095-1103.
[31] Ledford, W. K.; Kilbey, S. M. *Addit. Manuf.* **2023**, *63*, 103419.
[32] Dickson, A. N.; Barry, J. N.; McDonnell, K. A.; Dowling, D. P. *Addit. Manuf.* **2017**, *16*, 146-152.
[33] Trimble, A. Z.; Nejhad, M. N. G. *Woodhead Publ. Ser. Compos. Sci. Eng.* **2020**, *2*, 87-113.
[34] Street, D. P.; Mah, A. H.; Patterson, S.; Pickel, D. L.; Bergman, J. A.; Stein, G. E.; Messman, J. M.; Kilbey, S. M. *Polymer* **2018**, *157*, 87-94.
[35] Street, D. P.; Mah, A. H.; Ledford, W. K.; Patterson, S.; Bergman, J. A.; Lokitz, B. S.; Pickel, D. L.; Messman, J. M.; Stein, G. E.; Kilbey, S. M. *ACS Appl. Poly. Mater.* **2020**, *2*, 1312-1324.
[36] Perryman, S. C.; Dadmun, M. D. *Addit. Manuf.* **2021**, *38*, 101746.
[37] Levenhagen, N. P.; Dadmun, M. D. *ACS Appl. Polym. Mater.* **2019**, *1*, 876-884.
[38] Levenhagen, N. P.; Dadmun, M. D. *Polymer* **2018**, *152*, 35-41.
[39] Kanabenja, W.; Passarapark, K.; Subchokpool, T.; Nawaaukkaratharnant, N.; Roman, A. J.; Osswald, T. A.; Aumnate, C.; Potiyaraj, P. *Addit. Manuf.* **2022**, *59,* 103130.
[40] Bajwa, D.; Eichers, M.; Shojaeiarani, J.; Kallmeyer, A. *Ind. Crops. Prod.* **2021**, *173,* 114132.
[41] Lyu, Y.; Chen, Y. L.; Lin, L. Y.; Schlarb, A. K.; Li, Y.; Shi, X. Y. *Polym. Test.* **2022**, *106*, 107456.
[42] Peng, F.; Zhao, Z. Y.; Xia, X. H.; Cakmak, M.; Vogt, B. D. *ACS Appl. Mater. Interfaces* **2018**, *10*, 16087-16094.
[43] Hart, K. R.; Dunn, R. M.; Wetzel, E. D. *Adv. Eng. Mater.* **2020**, *22*, 1901184.
[44] Koker, B.; Ruckdashel, R.; Abajorga, H.; Curcuru, N.; Pugatch, M.; Dunn, R.; Kazmer, D. O.; Wetzel, E. D.; Park, J. H. *Addit. Manuf* .**2022**, *55*, 102807.
[45] Ai, J. R.; Peng, F.; Joo, P.; Vogt, B. D. *ACS Appl. Polym. Mater.* **2021**, *3*, 2518-2528.
[46] Naqi, A.; Swain, Z.; Mackay, M. E. *ACS Appl. Polym. Mater.* **2023**, *5*, 2481-2489.
[47] Ai, J.-R.; Li, S.; Vogt, B. D. *Addit. Manuf.* **2022**, *60*, 103209.
[48] Kim, H.-C.; Kim, D.-Y.; Lee, J.-E.; Park, K. *Adv. Mater. Lett.* **2017**, *8*, 1199-1203.
[49] Szust, A.; Adamski, G. *Eng. Failure Anal.* **2022**, *132*, 105932.
[50] Basgul, C.; Yu, T.; MacDonald, D. W.; Siskey, R.; Marcolongo, M.; Kurtz, S. M. *J. Mech. Behav. Biomed. Mater.* **2020**, *102*, 103455.
[51] Chen, W. H.; Zhang, X. L.; Tan, D.; Xu, P.; Yang, B. S.; Shi, K.; Zhu, B.; Liu, Q.; Lei, Y. F.; Liu, S.; Xue, L. J. *Macromol. Rapid Commun.***2022**, *43,* e2100874.
[52] De Avila, E.; Eo, J.; Kim, J.; Kim, N. P. *MATEC Web of Conferences* **2019**, *264*, 02001.
[53] Levenhagen, N. P.; Dadmun, M. D. *Polymer* **2017**, *122*, 232-241.
[54] Stürzel, M.; Hees, T.; Enders, M.; Thomann, Y.; Blattmann, H.; Mülhaupt, R. *Macromolecules* **2016**, *49*, 8048-8060.
[55] Lourinho, C.; Salgado, H.; Correia, A.; Fonseca, P. *Biomedicines* **2022**, *10*, 2565.
[56] Das, A.; Gilmer, E. L.; Biria, S.; Bortner, M. J. *ACS Appl. Poly. Mater.* **2021**, *3*, 1218-1249.
[57] Arrigo, R.; Frache, A. *Polymers* **2022**, *14*, 1754.
[58] Coogan, T. J.; Kazmer, D. O. *J. Rheol.* **2019**, *63*, 141-155.
[59] Nguyen, N. A.; Bowland, C. C.; Naskar, A. K. *Appl. Mater. Today* **2018**, *12*, 138-152.
[60] Cox, W. P.; Merz, E. H. *J. Polym. Sci* .**1958**, *28*, 619-622.
[61] Huang, C.-C.; Liu, C.-Y. *Polymer* **2021**, *225*, 123760.
[62] Racin. R; Brouge, D. C. *J. Rheol* .**1979**, *23*, 263-280.

[63] Tordella, J. P. *J. Rheol.* **1957**, *1*, 203-212.
[64] Wu, S.; Beckerbauer, R. *Polymer J.* **1992**, *24*, 1437-1442.
[65] Liu, J.; Zhao, Z.; Wang, W.; Mays, J. W.; Wang, S. Q. *J. Polym. Sci. B: Polym. Phys.* **2019**, *57*, 758-770.
[66] Kusy, R. P.; Katz, M. J. *J. Mater. Sci.* **1976**, *11*, 1475-1486.
[67] Gilmer, E. L.; Miller, D.; Chatham, C. A.; Zawaski, C.; Fallon, J. J.; Pekkanen, A.; Long, T. E.; Williams, C. B.; Bortner, M. J. *Polymer* **2018**, *152*, 51-61.
[68] Bellini, A.; Gu¨c¸eri , S. u.; Bertoldi, M. *J. Manuf. Sci. Eng.* **2004**, *126*, 237-246.
[69] Chen, J.; Smith, D. E. *Addit. Manuf.* **2021**, *47*, 102208.
[70] Liu, R. C. W.; Morishima, Y.; Winnik, F. M. *Polymer J.* **2002**, *35*, 340-346.
[71] Ishiyama, C.; Higo, Y. *J .Polym. Sci.B: Polym. Phys.* **2002**, *40*, 460-465.
[72] *AZONetwork*: AZO Materials, **2001**
[73] Holt, D. L. *J. Appl. Polym. Sci.* **1968**, *12*, 1653-1659.
[74] Gupta, A.; Alifui-Segbaya, F.; Hasanov, S.; White, A. R.; Ahmed, K. E.; Love, R. M.; Fidan, I. *J. Mech. Behav. Biomed. Mater.* **2023**, *143*, 105950.

Sierra F. Yost, Christian W. Pester, Bryan D. Vogt*

Molecular Mass Engineering for Filaments in Material Extrusion Additive Manufacture

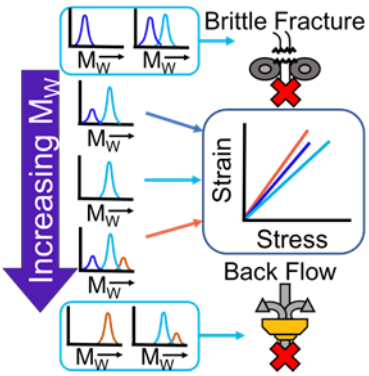

Tailoring polymer molecular weight distribution poly(methyl methacrylate) increases the mechanical properties of 3D printed objects. Bimodal and trimodal M_w distributions are examined to elucidate how details impact rheology, printability and printed part performance. Printability can be estimated from combination of flow identification number and minimum radius of curvature of the filament prior to failure.

.

Supporting Information

Molecular Mass Engineering for Filaments in Material Extrusion Additive Manufacture

*Sierra F. Yost[1], Christian W. Pester[1,2,3], Bryan D. Vogt[1]**

S. F. Yost, Prof. C. W. Pester, Prof. B. D. Vogt
[1]Department of Chemical Engineering, The Pennsylvania State University, University Park, PA 16802, United States
[2] Department of Materials Science and Engineering, The Pennsylvania State University, University Park, PA 16802, United States
[3] Department of Chemistry, The Pennsylvania State University, University Park, PA 16802, United States

E-mail: bdv5051@psu.edu (B.D.V.)

Additional experimental details

Gel Permeation Chromatography A GPC TOSOH EcoSEC HCL-8320 GPC system with a refractive index (RI) detector was used to determine molecular weight. Samples were dissolved into HPLC-grade tetrahydrofuran (THF) (1mg mL^{-1}) and filtered through a 0.2 μm polytetrafluoroethylene (PTFE) filter. The samples were run though TOSOH TSKgel GMHHR-H column (7.8 mm I.D x 30 cm) in the THF mobile phase at 1.0 mL min^{-1} at 40°C. Samples were analyzed with an RI detector at 254 nm and molecular weights are reported relative to PMMA standards.

Table S1. Nomenclature, molecular weight, and dispersity of PMMA blends with 78.3 kg mol^{-1} PMMA base. 38.4 kg mol^{-1} and 309.1 kg mol^{-1} are mixed at a ratio of 171:29.

Name	Weight Percent[a]	M_n (kg mol^{-1})	M_w (kg mol^{-1}) [b]	M_z (kg mol^{-1})	$Đ$
B100	100% 38.4/309.1 kg mol^{-1}	14.0	51.7	227.2	3.68
B50	50% 38.4/309.1 kg mol^{-1}	23.1	75.5	252.9	3.27
B20	20% 38.4/309.1 kg mol^{-1}	29.7	70.2	147.2	2.37
B10	10% 38.4/309.1 kg mol^{-1}	32.1	71.9	152.0	2.24
L20	20% 38.4 kg mol^{-1}	21.3	65.5	160.6	3.08
L10	10% 38.4 kg mol^{-1}	27.5	71.2	133.4	2.59
M20	20% 70.3 kg mol^{-1}	26.1	63.2	181.8	2.42
M10	10% 70.3 kg mol^{-1}	27.0	71.2	175.2	2.636
H20	20% 309.1 kg mol^{-1}	38.3	131.8	335.8	3.43
H10	10% 309.1 kg mol^{-1}	30.6	87.4	217.1	2.86

[a] remainder of the blend composition is 78.3 kg mol^{-1} PMMA.
[b] as determined by GPC

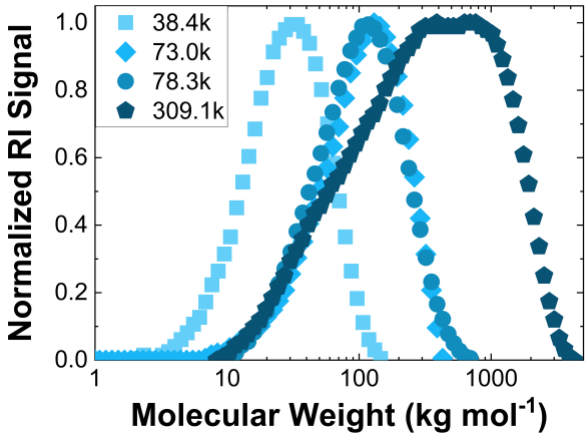

Figure S1. GPC traces for PMMA polymers examined.

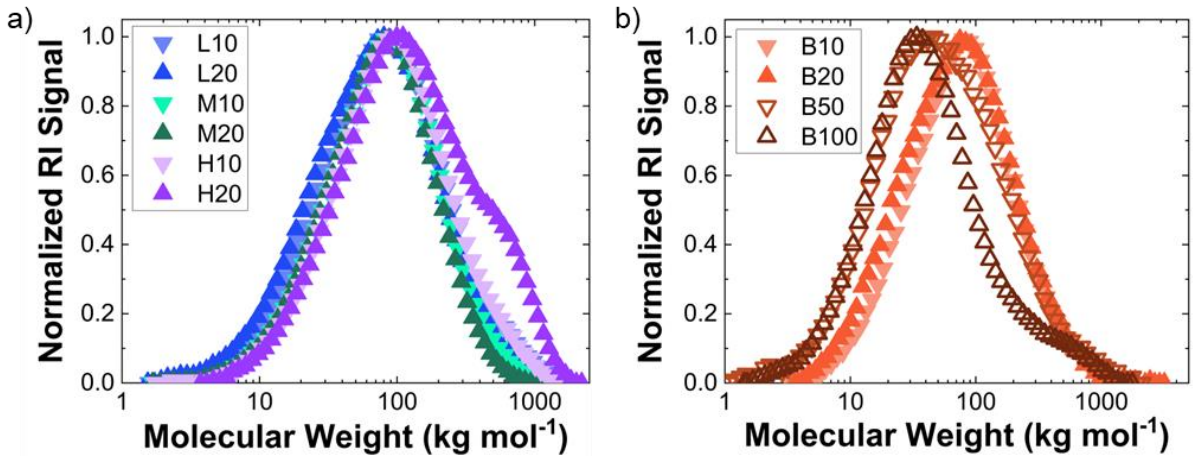

Figure S2. GPC traces for a) binary (L10, L20, M10, M20, H10, and H20) and b) ternary (B10, B20, B50, and B100) blends of the PMMA shown in Figure S1.

Table S2. Diameter for the filaments examined.

Sample Name	Diameter (mm)
78.3 kg mol^{-1}	1.71 ± 0.03
73.0 kg mol^{-1}	1.79 ± 0.04
L10	1.81 ± 0.02
L20	1.79 ± 0.03
M10	1.82 ± 0.01
M20	1.73 ± 0.04
B10	1.81 ± 0.07
B20	1.84 ± 0.03

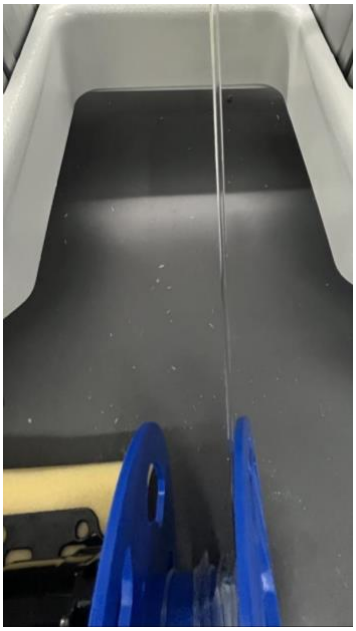

Figure S3: Filament extrusion and winding of L10 sample.

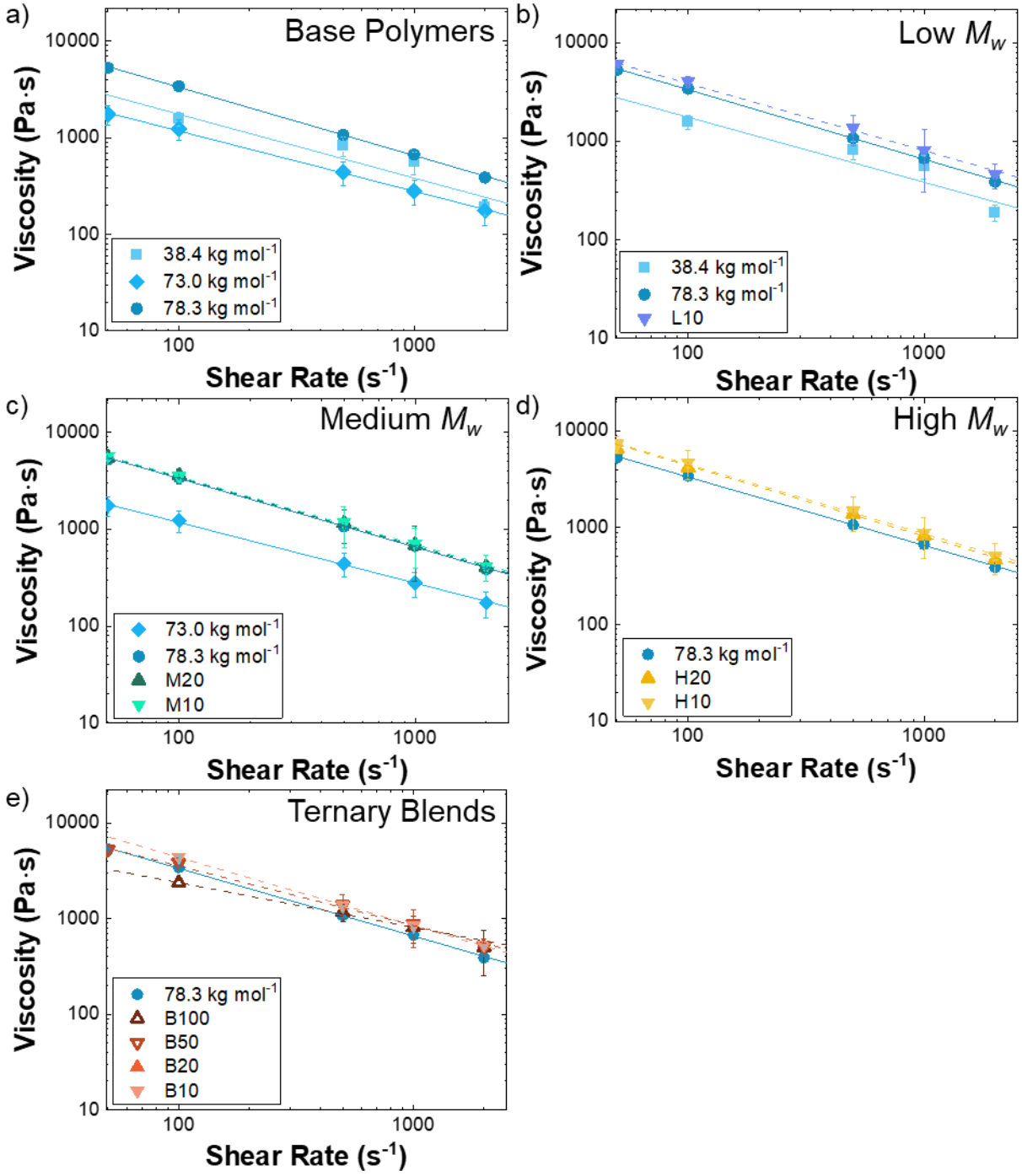

Figure S4. Viscosity at 200°C of PMMA a) base polymers and blends b) low M_w L10/L20 with 78.3 kg mol^{-1}, c) medium M_w M10/M20 with 78.3 kg mol^{-1}, d) high M_w H10/H20, and e) ternary blend B10/B20/B50/B100 with 78.3 kg mol^{-1}. The dashed lines are best fits to a power law model.

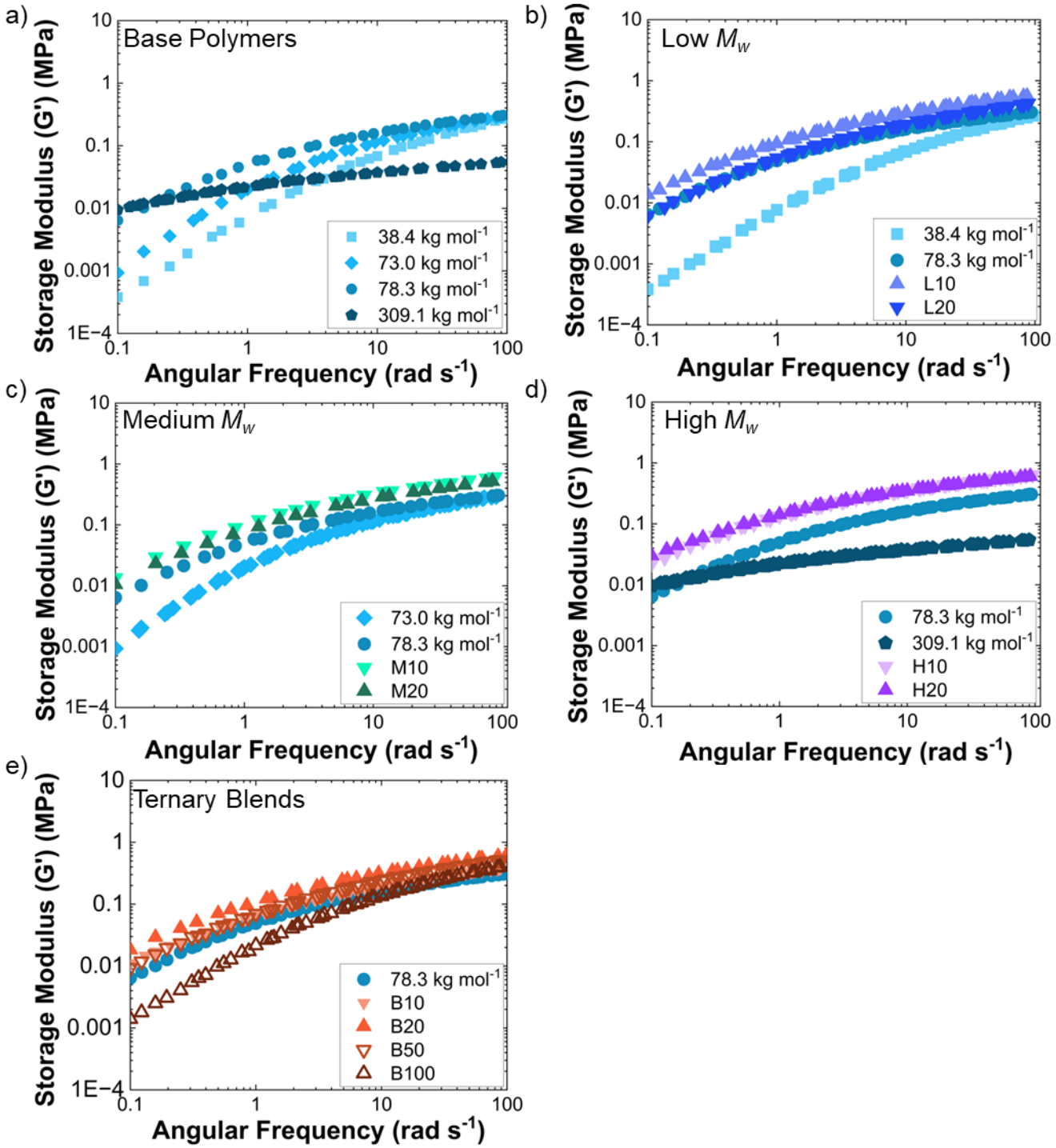

Figure S5. Storage modulus (G') vs. angular frequency (ω) for **a)** base PMMA samples, **b)** low M_w (L10 and L20) with 78.3 kg mol^{-1}, **c)** medium M_w (M10 and M20) with 78.3 kg mol^{-1}, **d)** high M_w (H10 and H20) with 78.3 kg mol^{-1}, and **e)** ternary blend (B10, B20, B50, and B100) with 78.3 kg mol^{-1}.

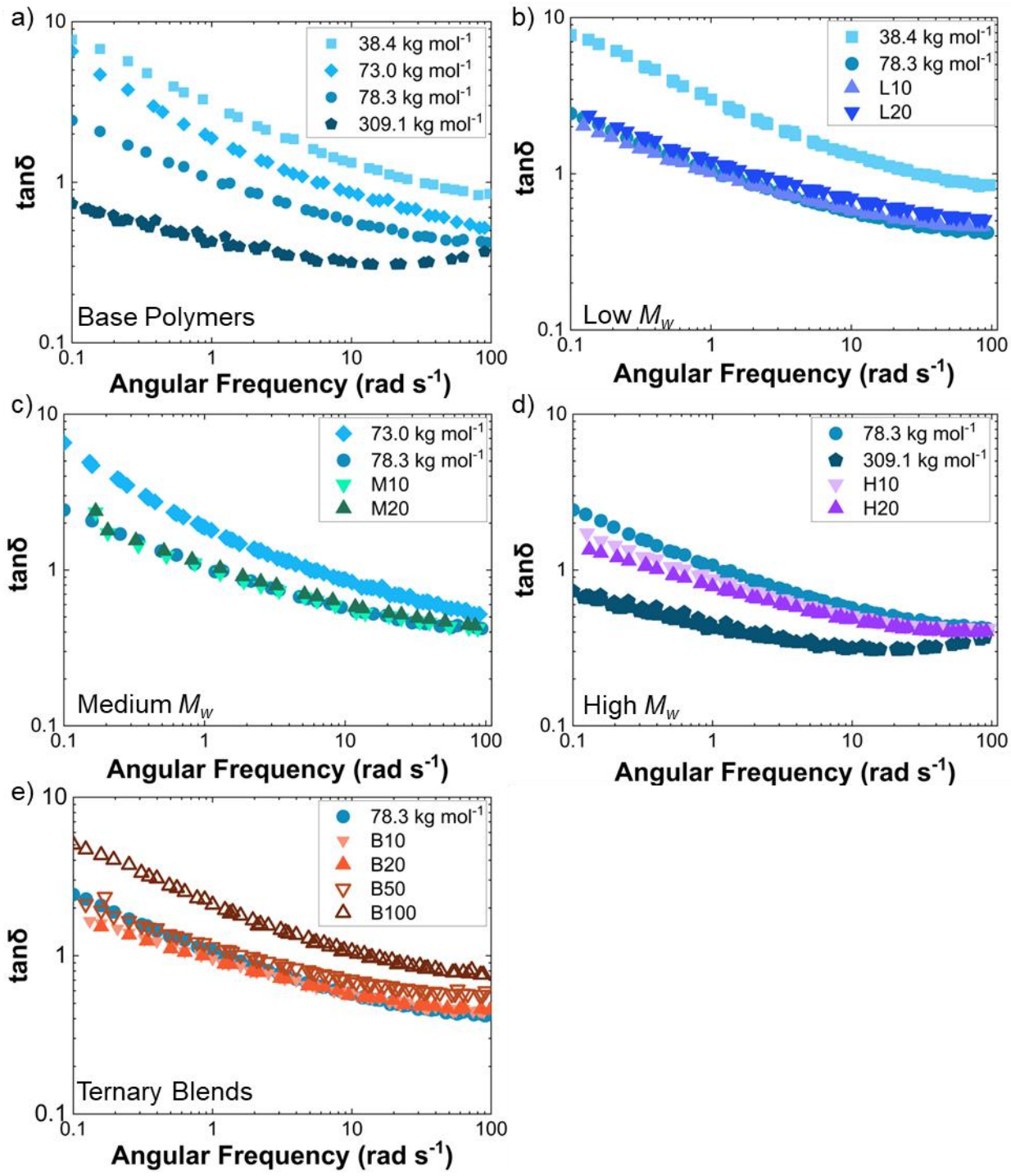

Figure S6. Loss modulus (*tanδ) as a function of* angular frequency (ω) for **a)** base PMMA, **b)** low M_w (L10 and L20) with 78.3 kg mol^{-1}, **c)** medium M_w (M10 and M20) with 78.3 kg mol^{-1}, **d)** high M_w (H10 and H20) with 78.3 kg mol^{-1}, and **e)** ternary blend (B10, B20, B50, and B100) with 78.3 kg mol^{-1}.

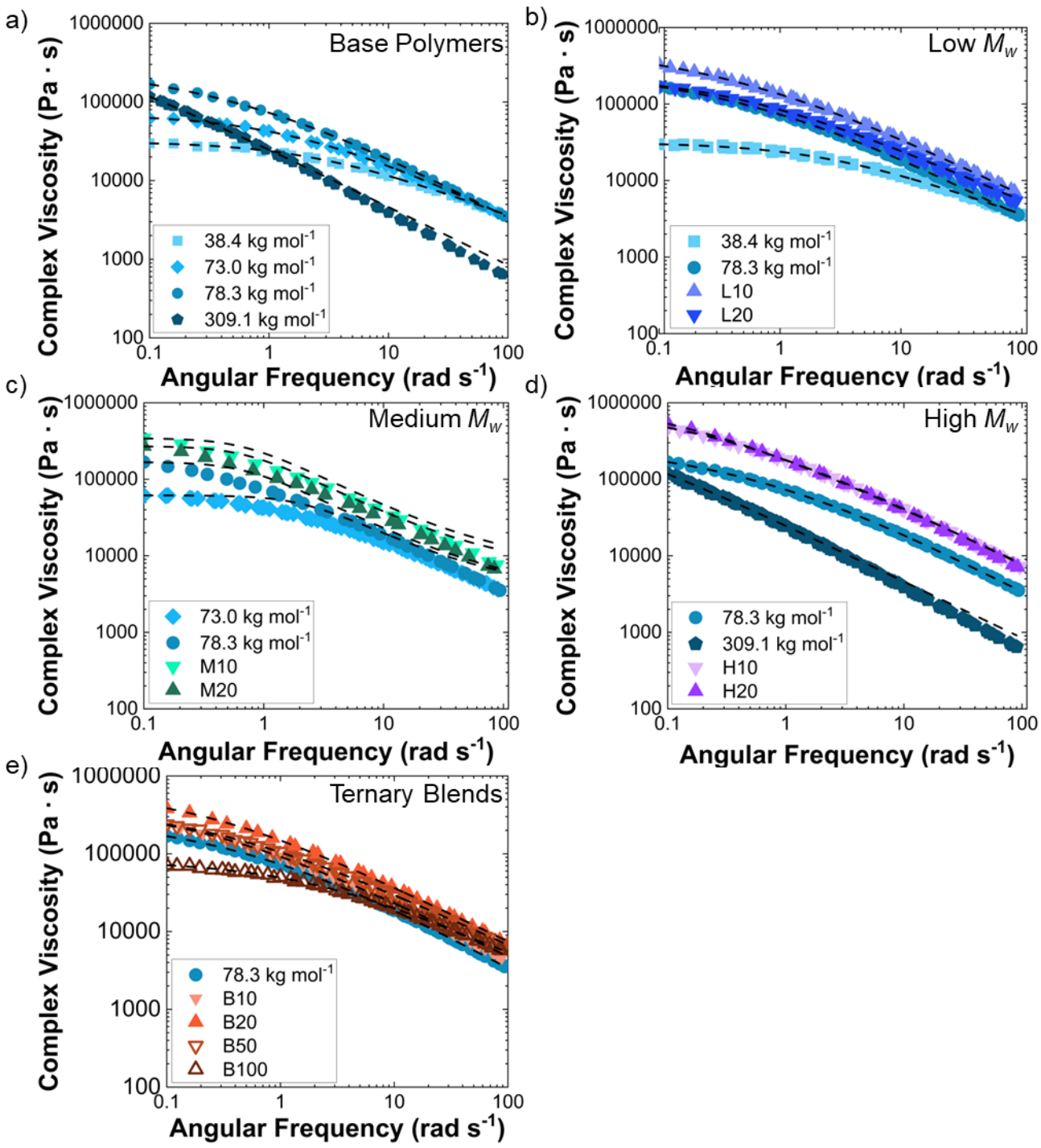

Figure S7. Complex viscosity vs. angular frequency for **a)** base PMMA, **b)** low M_w (L10 and L20) with 78.3 kg mol^{-1}, **c)** medium M_w (M10 and M20) with 78.3 kg mol^{-1}, **d)** high M_w (H10 and H20) with 78.3 kg mol^{-1}, and **e)** ternary blend (B10, B20, B50, and B100) with 78.3 kg mol^{-1}. Fits of the data to Carreau-Yasuda model for all samples are denoted by black dashed lines.

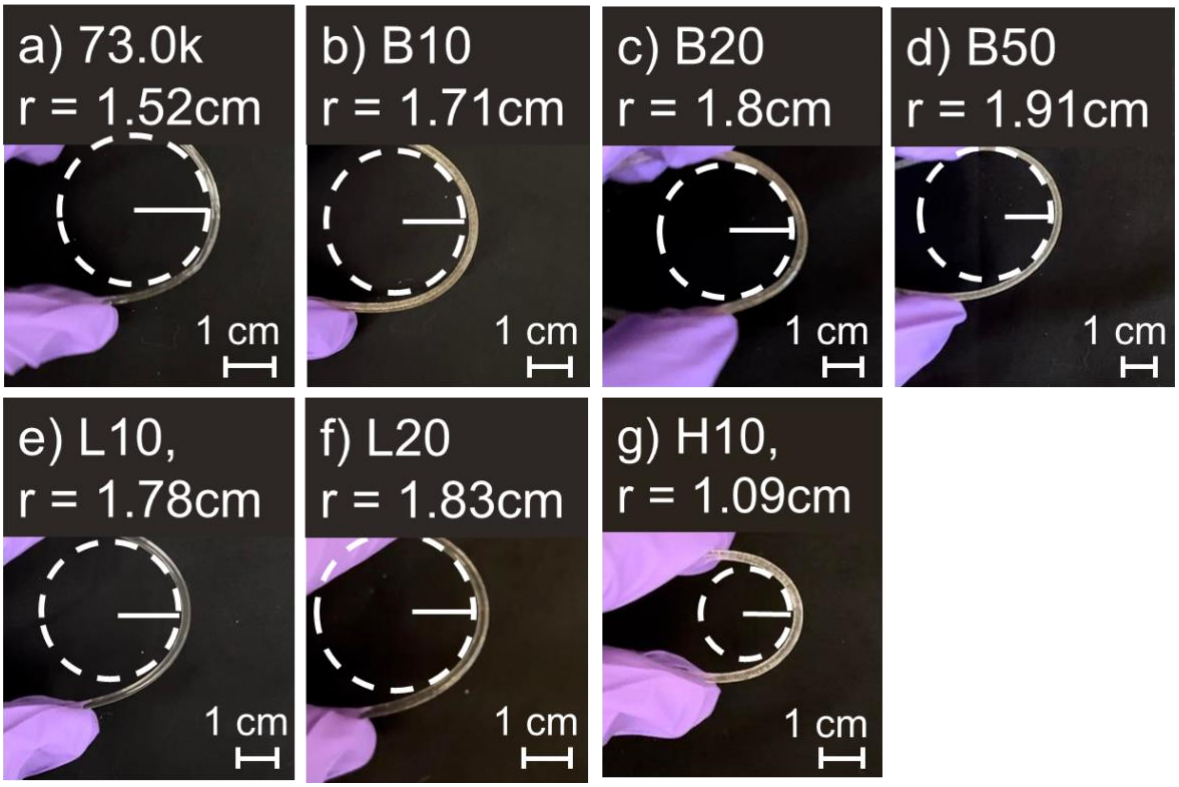

Figure S8. Photographs of PMMA filaments at maximum curvature obtainable prior to failure of; the largest curvature is shown for **a)** 73.0 kg mol^{-1} PMMA, **b)** B10, **c)** B20, **d)** B50, **e)** L10, **f)** L20 and **g)** H10. The radius of curvature is listed in the panel.

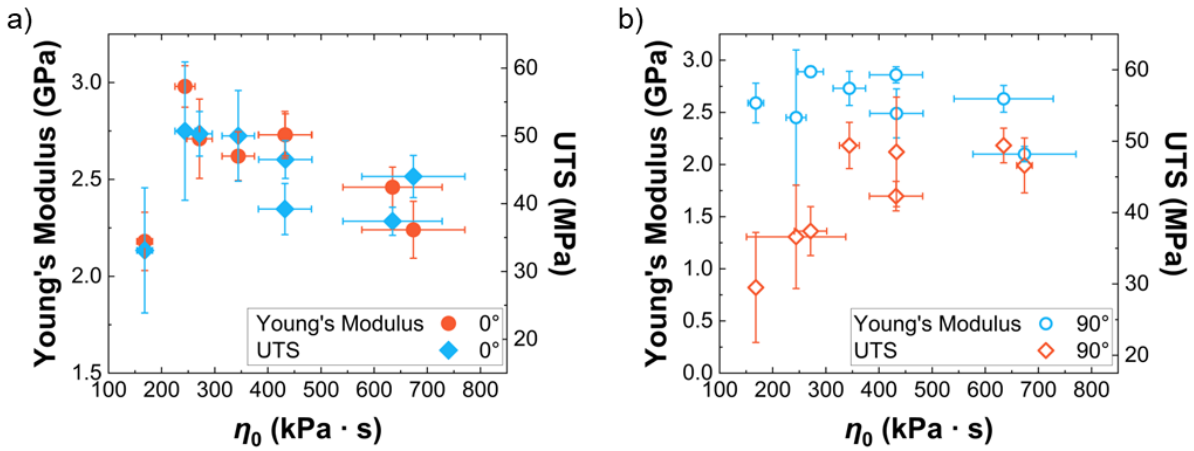

Figure S9. Young's modulus and ultimate tensile strength vs. zero-shear viscosity. **a)** closed symbols indicate a raster angle 0° to the direction of tensile testing and **b)** open symbols indicate a raster angle 90° to the direction of tensile testing.

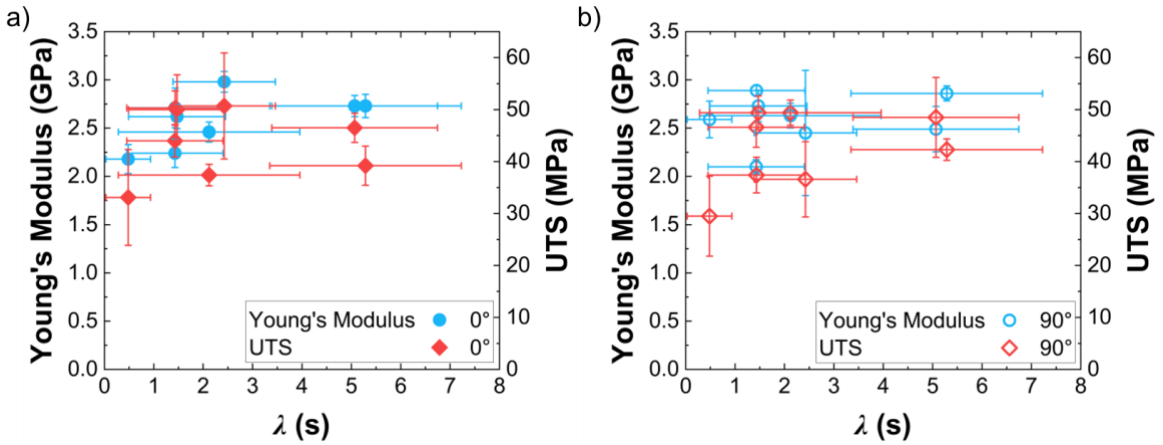

Figure S10. Young's modulus and ultimate tensile strength vs. characteristic time (λ) determined from the Carreau-Yasuda fit. **a)** closed symbols indicate a raster angle 0° to the direction of tensile testing and **b)** open symbols indicate a raster angle 90° to the direction of tensile testing.

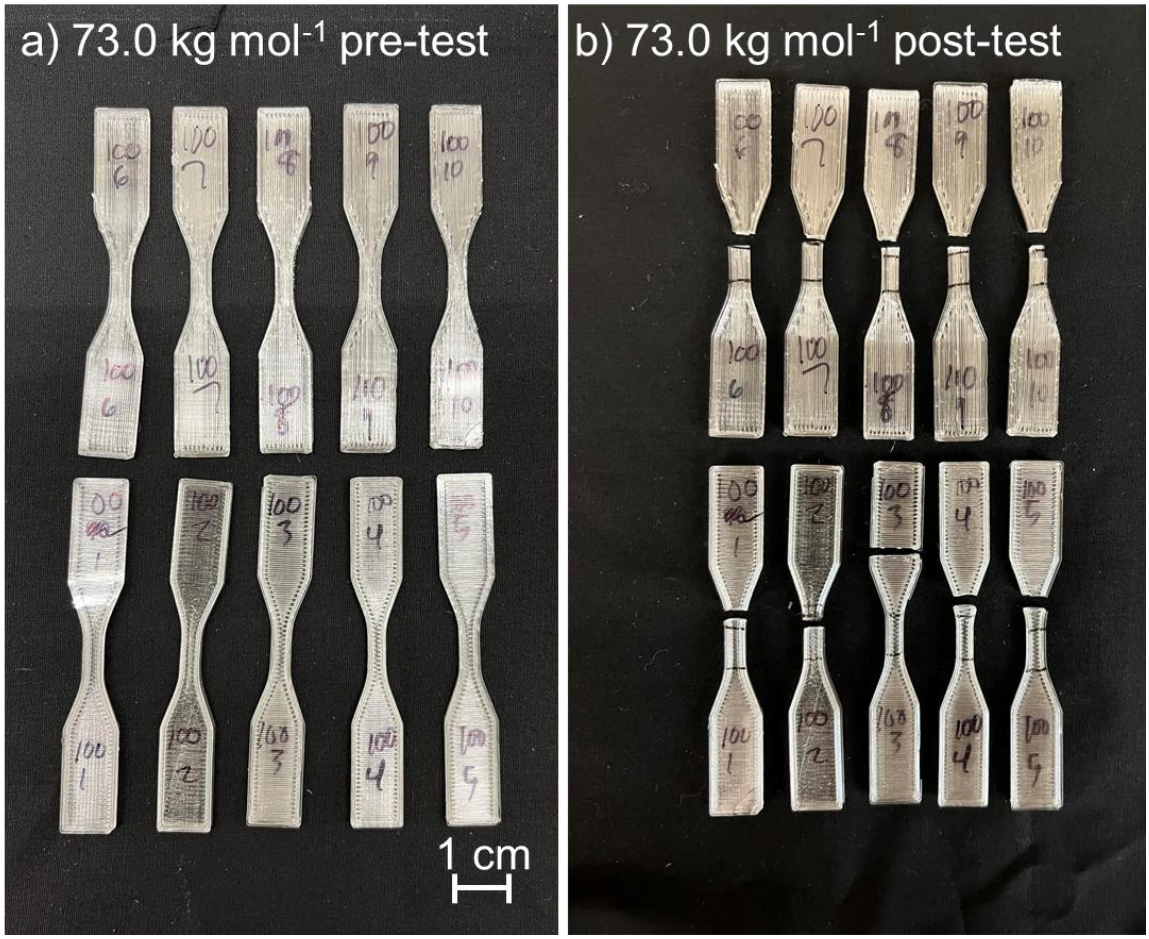

Figure S11 73.0 kg mol^{-1} 3D printed Type V tensile bars a) pre- and b) post-tensile test, bottom tests are 90° raster angle, top tests are 0° raster angle.

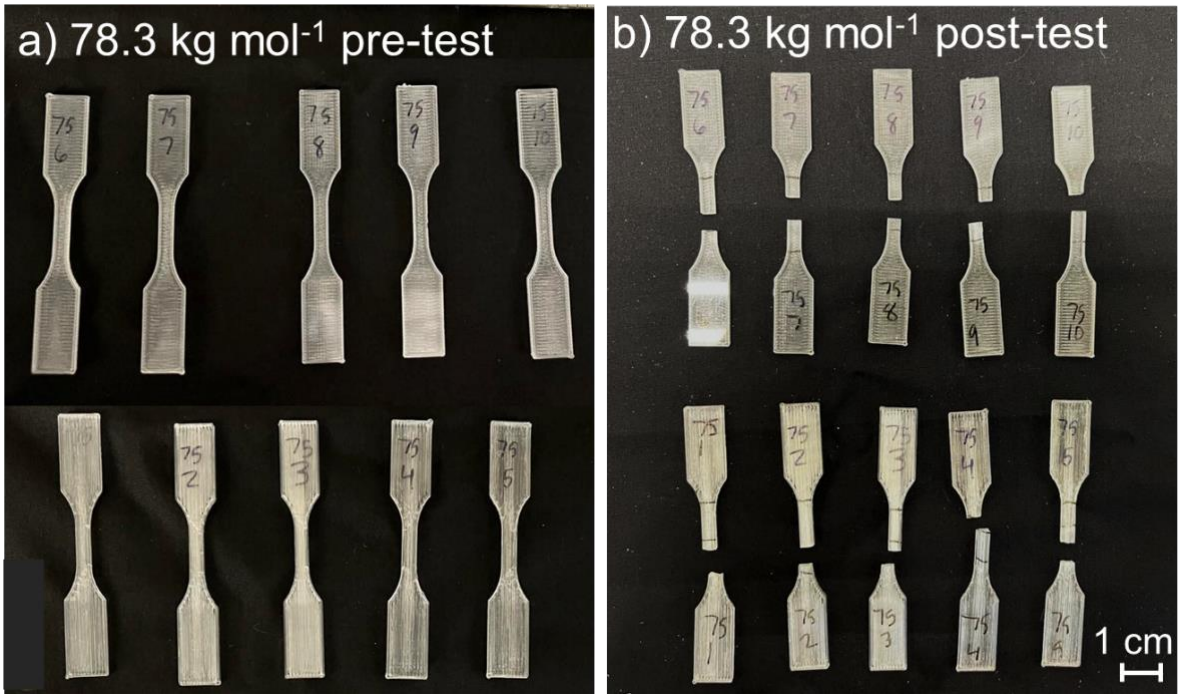

Figure S12. 78.3 kg mol^{-1} 3D printed Type V tensile bars **a)** pre- and **b)** post-tensile test, bottom tests are 0° raster angle, top tests are 90° raster angle.

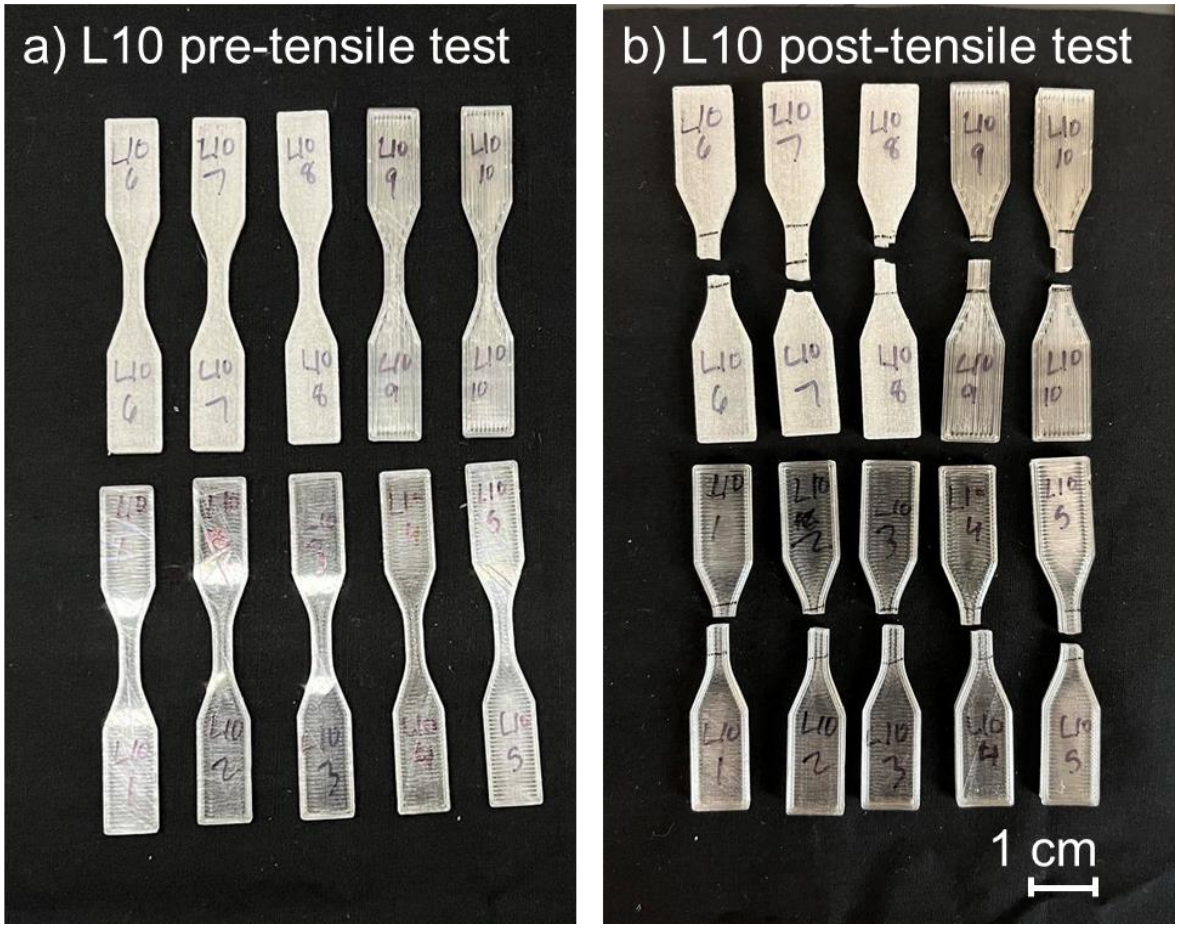

Figure S13. L10 samples 3D printed Type V tensile bars **a)** pre- and **b)** post-tensile test, bottom tests are 90° raster angle, top tests are 0° raster angle.

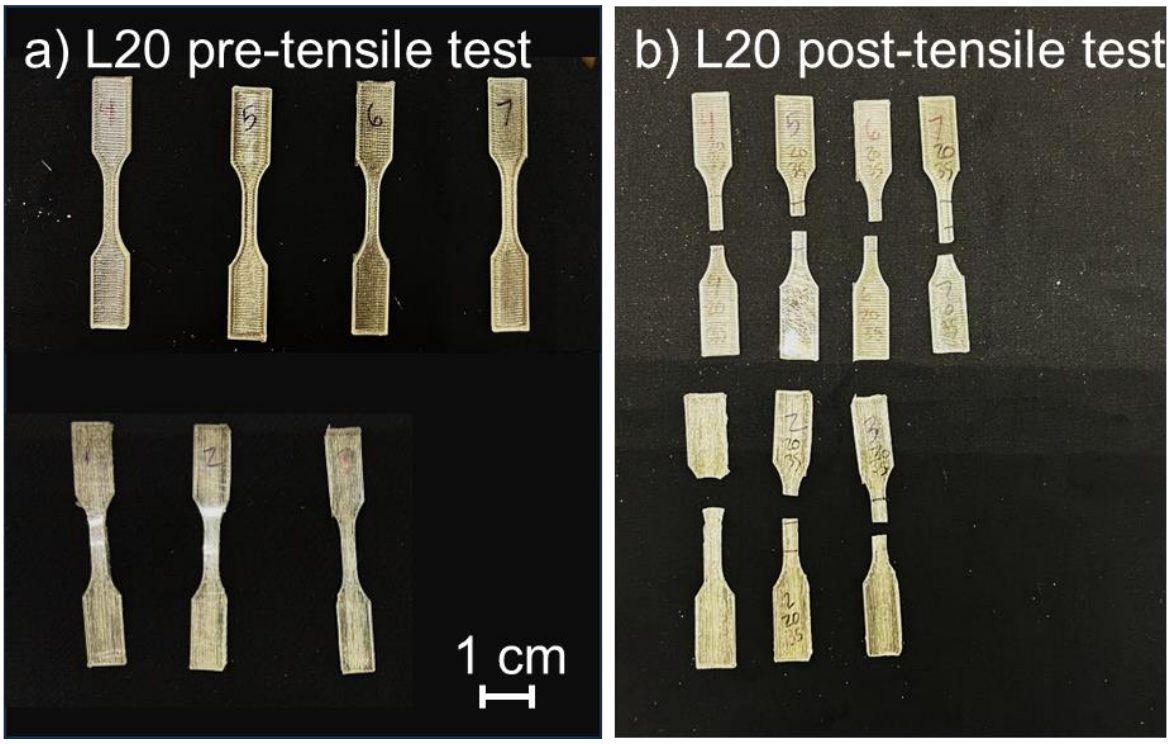

Figure S14. L20 samples 3D printed Type V tensile bars **a)** pre- and **b)** post-tensile test, bottom tests are 90° raster angle, top tests are 0° raster angle.

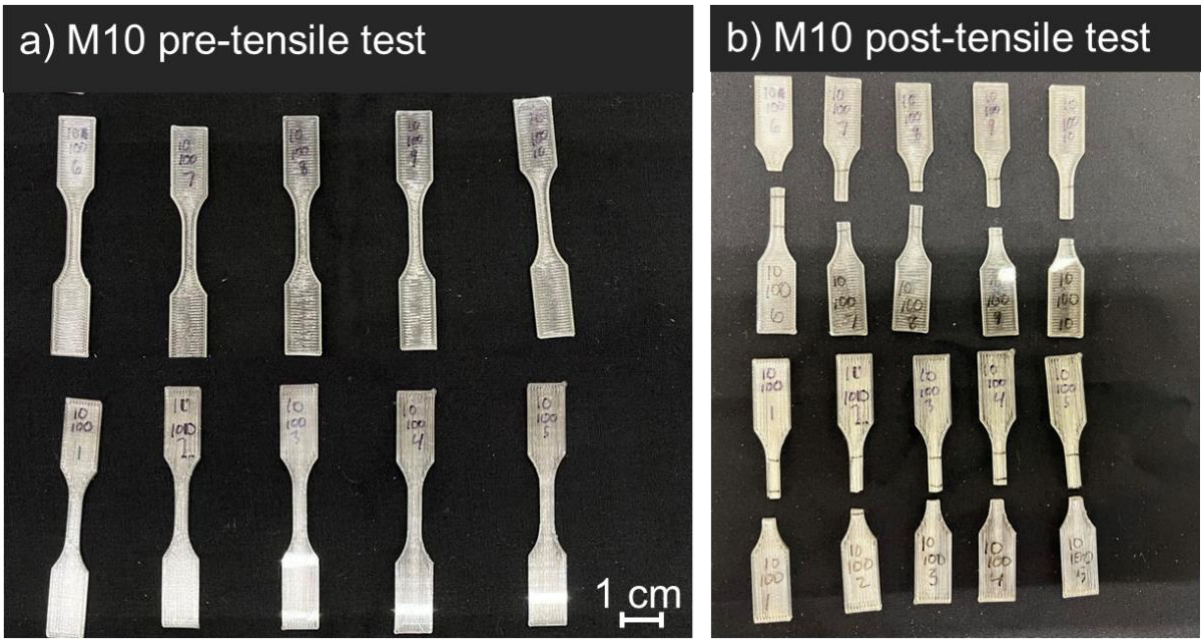

Figure S15. M10 samples 3D printed Type V tensile bars **a)** pre- and **b)** post-tensile test, bottom tests are 0° raster angle, top tests are 90° raster angle.

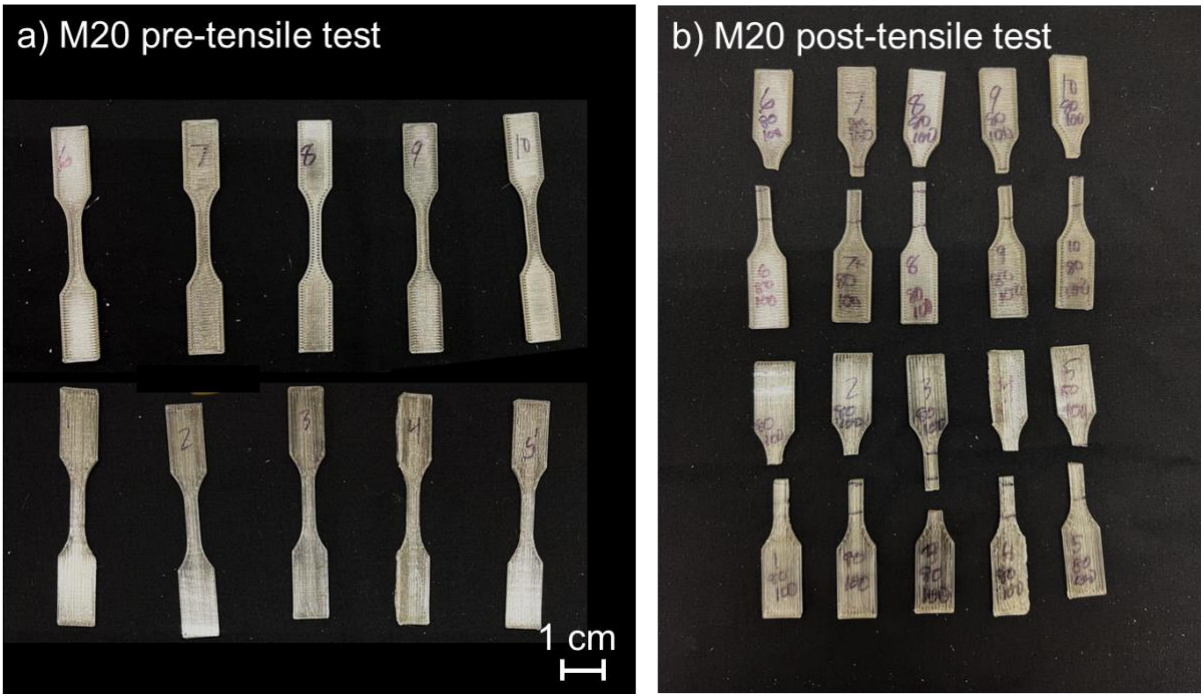

Figure S16. M20 samples 3D printed Type V tensile bars **a)** pre- and **b)** post-tensile test, bottom tests are 0° raster angle, top tests are 90° raster angle.

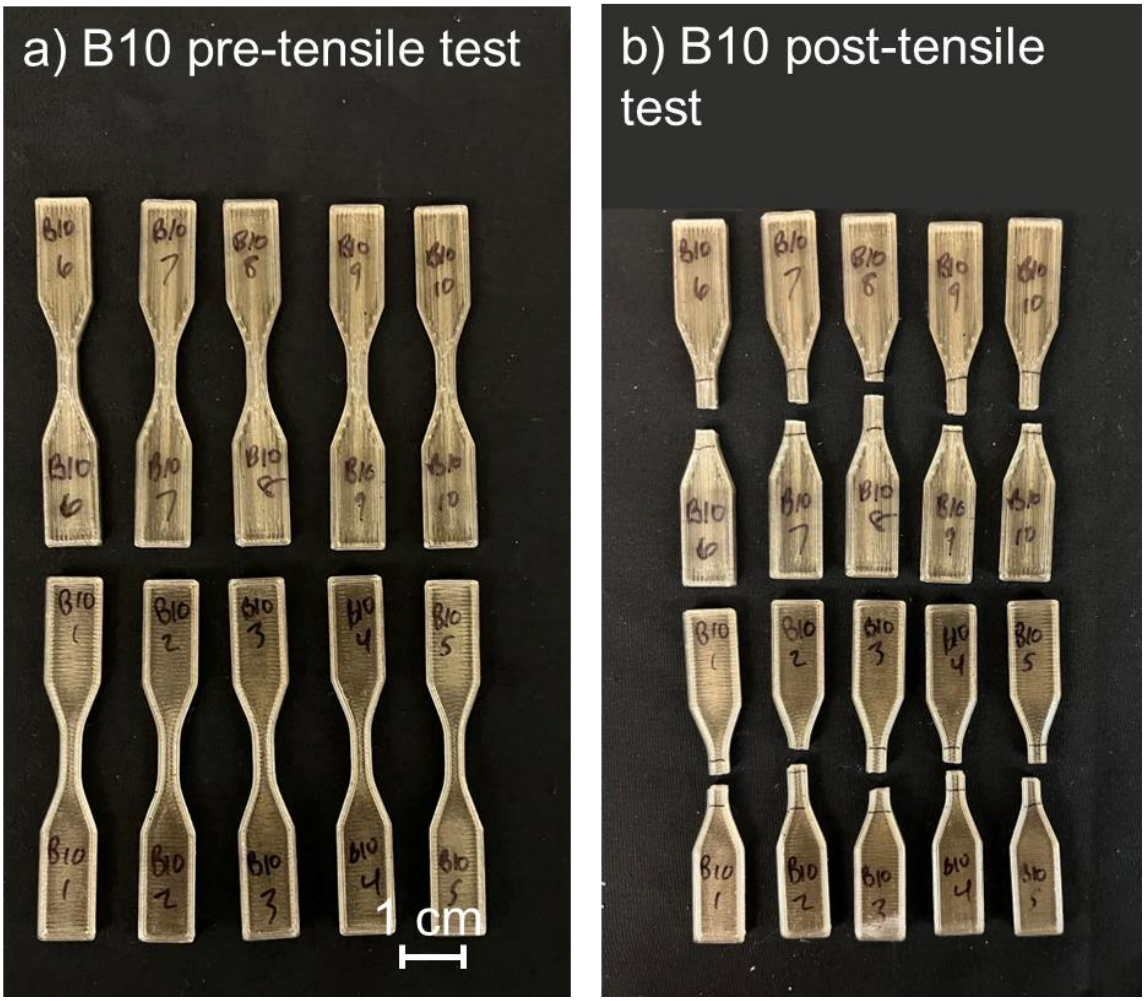

Figure S17. B10 samples 3D printed Type V tensile bars **a)** pre- and **b)** post-tensile test, bottom tests are 90° raster angle, top tests are 0° raster angle.

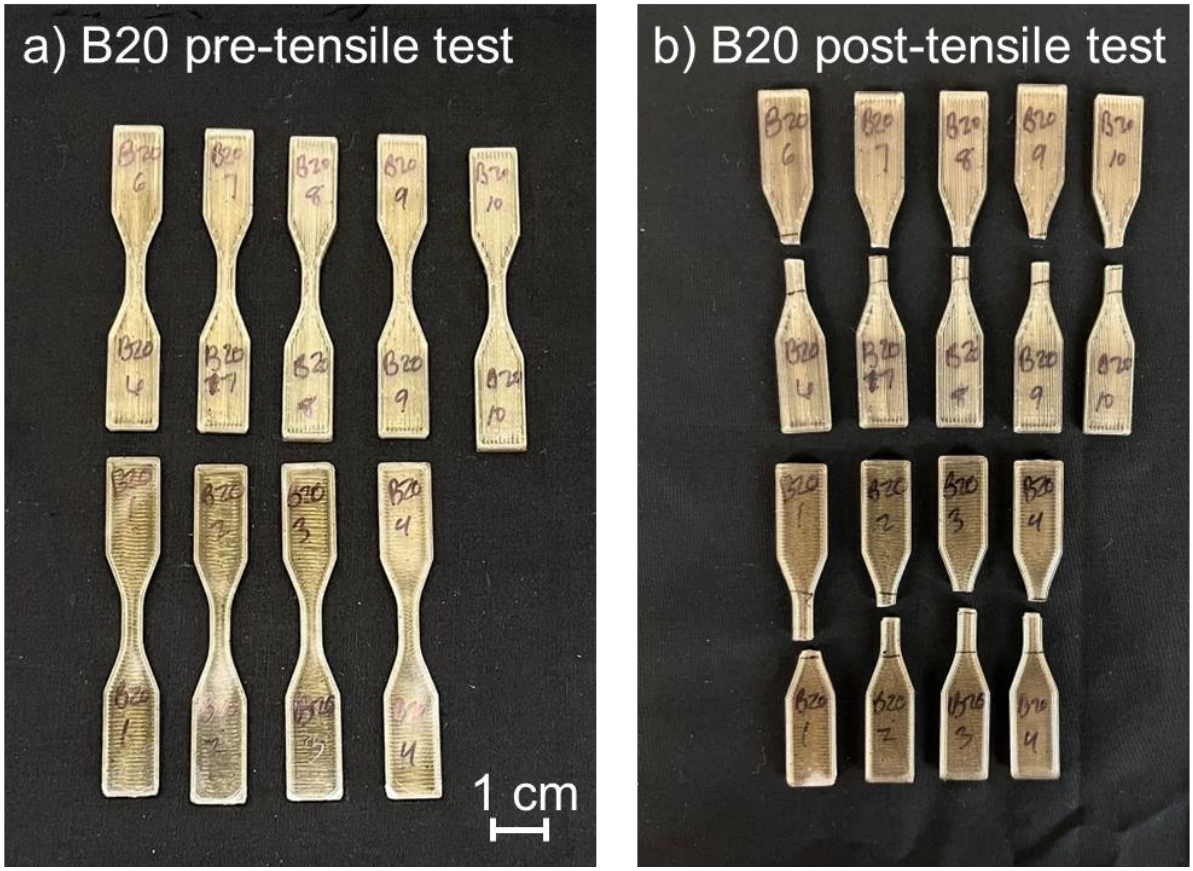

Figure S18. B20 samples 3D printed Type V tensile bars **a)** pre- and **b)** post-tensile test, bottom tests are 90° raster angle, top tests are 0° raster angle.

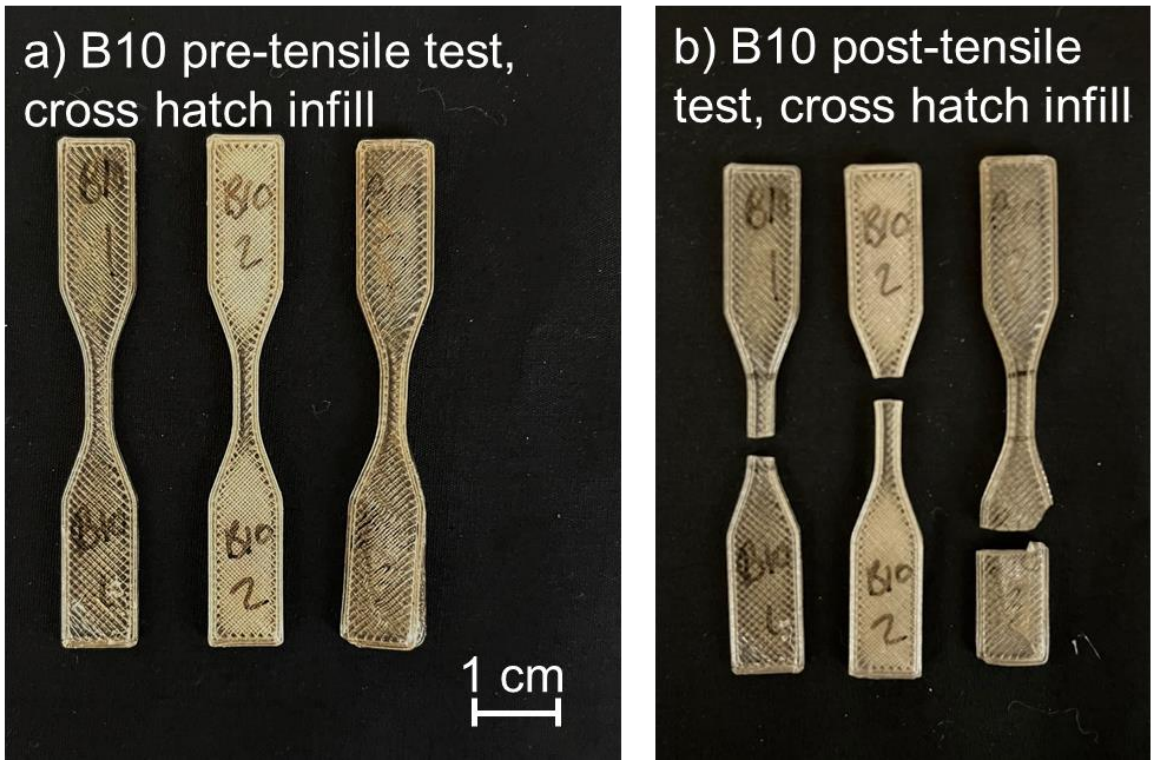

Figure S19. B10 samples 3D printed Type V tensile bars with a 45°/-45° crosshatching pattern **a)** pre- and **b)** post-tensile test.